國立臺灣大學工學院工程科學及海洋工程學系

碩士論文

Department of Engineering Science and Ocean Engineering

College of Engineering

National Taiwan University

Master Thesis

基於船舶減阻之小水線面雙體船水下胴體設計優化

The Pontoon Design Optimization of a SWATH Vessel for Resistance Reduction

吳濟民

Chi-Min Wu

指導教授：趙修武 博士

Advisor: Dr.-Ing. Shiu-Wu Chau

中華民國 112 年 6 月

June, 2023

doi:10.6342/NTU202304123

Abstract

This study employs a deep neuron network (DNN) model to optimize the 22.5 m long pontoon hull form of a small water-plane area twin hull (SWATH) vessel with fin stabilizer for reducing its calm water resistance at $F_r = 0.8$ under an even keel condition. The resistance of the target vessel is linearized into three components, i.e., pontoon, strut, and fin stabilizer, to simplify the resistance calculation. Four design parameters, i.e., the length of the fore-body and aft-body, the angle of fore body and aft body, are used to define the geometry of pontoon. The computational fluid dynamics (CFD) software STAR-CCM+ is used to predict the resistance of the underwater pontoon as well as the lift and drag force of the fin stabilizer at different angles of attack. Then, a deep neural network model is trained with 1400 CFD resistance predictions using MATLAB, and K-fold cross-validation is used to ensure the DNN model stability and search for the optimized design parameter set. The proposed DNN model has 6, 8, 9, 8, and 7 neurons in five hidden layers, respectively. The optimized design parameters are the length of the fore-body 7.8 m, the length of the aft-body 6.8 m, fore body angle 10°, and the aft body angle 35°. This study finds that the resistance reduction of the optimized design compared to the baseline design is mainly due to the small angle of attack of fin stabilizers where the optimized pontoon results in a small Munk moment to be balanced by the fin stabilizer. The optimized pontoon design is able to reduce the resistance by 2.2% compared to the baseline design.

Keywords: SWATH, Pontoon, Resistance, Hull Form, Optimization, CFD, Deep Neural Network.

doi:10.6342/NTU202304123

摘要

本研究藉由深度神經網路模型尋找優化的 22.5 公尺水下胴體船形設計，藉此降低具穩定翼小水面雙體船在平浮條件下$F_r = 0.8$的靜水阻力。本研究將小水線面雙體船的阻力線性化為浮筒、支架和穩定翼阻力，藉此簡化整體阻力的計算。本研究使用 4 個船形參數定義水下浮筒外形，分別為浮筒前段長度、浮筒後段長度、浮筒入水角及浮筒出水角。本研究使用計算流體力學軟體 STAR-CCM+預測水下胴體完全沒水阻力，以及計算穩定翼在不同攻角下的升阻力。接著使用 MATLAB 數學軟體與 1400 個 CFD 阻力預測結果訓練深度神經網路模型，通過 K-fold 交叉驗證確保模型的穩定性，並尋找優化的船形參數組合。本研究所提出的深度神經網路模型包含五個隱藏層，每個隱藏層的神經元數量分別為 6、8、9、8 和 7。本研究建議的優化設計參數為浮筒前段長度 7.8 m，浮筒後段長度 6.8 m，前段角度 10°，後段角度 35°。本研究發現相較於原始船形，優化設計船形的減阻效應主要來自水下胴體產生的孟克力矩較小，使得所需穩定翼的攻角較小。由於小水線面雙體船依靠穩定翼平衡船體生成的孟克力矩，因此穩定翼攻角減少，導致穩定翼阻力大幅降低。使用本研究建議的優化水下胴體設計，總阻力相較於原始船形減少 2.2%。

關鍵詞：小水面雙體船，水下胴體，阻力，船形，優化，計算流體力學，深度神經網路

doi:10.6342/NTU202304123

Contents

doi:10.6342/NTU202304123

Nomenclature

Latin symbols

A_{pn}^{∞}	The surface area of the pontoon	[m^2]
B_{OA}	Beam over all	[m]
b_j^{hl}	Bias of the hidden layer	[-]
C_L	Lift coefficient	[-]
C_a	Volume fraction of air	[-]
C_w	Volume fraction of water	[-]
C_α	Sharpening factor	[-]
C_q	Transfer-flow resistance coefficient of rudder	[-]
$c_{\varepsilon 1}$	Equation Constant	[-]
$c_{\varepsilon 2}$	Equation Constant	[-]
c_μ	Equation Constant	[-]
D	Ship Depth	[m]
D_p	Diameter of propeller	[m]
d	Draught	[m]
dx	Cell size of grid	[-]
E_ϕ	Discretization error	[-]
Fr	Froude number	[-]
F_{sta}	The lift force of fin stabilizer	[kN]
F_f	The lift force of fore fin stabilizer	[kN]
F_a	The lift force of aft fin stabilizer	[kN]
G	Production rate due to Reynolds-stress tensor	[W/m^3]
G_k	Production rate due to Reynolds-stress tensor	[W/m^3]
g	Gravitational acceleration	[m/s^2]
K	Turbulence kinetic energy	[J/kg]
L_f	Length of fore body	[m]
L_G	Moment arm length of center of gravity	[m]

doi:10.6342/NTU202304123

L_m	Length of parallel middle body	[m]
L_a	Length of after body	[m]
L_{OA}	Length over all	[m]
L_{WL}	Length of water line	[m]
L_{pn}	Length of pontoon	[m]
L_{fin}	Lift force of fin stabilizer	[kN]
M_T	Total moment	[kN·m]
M_{pitch}	The pitch moment of SWATH vessel	[kN·m]
M_{pn}^{∞}	Moment of pontoon in infinite water depth	[kN·m]
$M_{pn,p}^{\infty}$	Pressure moment of pontoon in infinite water depth	[kN·m]
$M_{pn,s}^{\infty}$	Shear moment of pontoon in infinite water depth	[kN·m]
M_{pn}^{fs}	Moment of pontoon in free surface condition	[kN·m]
M_{st}^{fs}	Moment of strut in free surface condition	[kN·m]
m_j^{hl}	Input for net hidden layers	[-]
N	Number of grid	[-]
N_n	Number of nth grid	[-]
N_{n-1}	Number of $n-1$th grid	[-]
n_i	i-th input	[-]
$\mathbf{n}$	Normal vector of boundary	[-]
P	Purelin function	[-]
p	Total Pressure	[pa]
p_s	Hydrostatic Pressure	[pa]
p_{pn}^{∞}	The pressure on the surface of the pontoon	[pa]
R	Radius of pontoon	[m]
Re	Reynolds number	[-]
R_T	Total resistance of small water area twin hull vessel	[kN]
R_L	Resistance of SWATH vessel of lower hull	[kN]
R_{st}	Resistance of SWATH vessel of strut	[kN]
R_{ss}	Resistance of SWATH vessel of super structure	[kN]

R_{pn}	Resistance of SWATH vessel of pontoon	[kN]
R_{fin}	Resistance of SWATH vessel of fin stabilizer	[kN]
R_{pn}^{∞}	Resistance of SWATH vessel of pontoon in infinite water depth	[kN]
R_T^{DNN}	The total resistance of SWATH predicted by DNN model	[kN]
R_T^{CFD}	The total resistance of SWATH predicted by CFD solver	[kN]
r	Radial direction	[m]
T	Tansig function	[-]
U_i	Velocity direction in the *i* direction	[m/s]
$U_{d,a}$	Diffusion rate of the air phase	[m^2/s]
$U_{c,a}$	Boundary sharpening speed of the air phase	[m/s]
u	Velocity component in the z direction	[m/s]
u_i'	Variation of average velocity in the *i* direction	[m/s]
$\mathbf{U}$	Flow velocity	[m/s]
V	Total volume in a cell	[m^3]
V_a	Volume of air in a cell	[m^3]
V_w	Volume of water in a cell	[m^3]
V_s	Vessel speed	[m/s]
V_A^*	Normalize velocity of axial	[m/s]
V_R^*	Normalize velocity of radial	[m/s]
V_T^*	Normalize velocity of tangential	[m/s]
v	Velocity component in the r direction	[m/s]
v_i	Velocity of different component at propeller plane	[m/s]
w_{ij}^{hl}	Weight of hidden layer	[-]
w_{jk}^{ol}	Weight of output layer	[-]
x_i	Cartesian coordinate in the *i* direction	[m]
z	Axial direction	[m]

Greek symbols

α	The angle of attack	[°]
β	Coefficient of effect of free surface	[-]
$\dot{\gamma}$	Shear rate	[1/s]
δ	Heave	[m]
δ_{ij}	Unit tensor	[-]
ε	Dissipation rate of turbulent kinetic energy	[kg·m^2/s^3]
η	Free surface elevation	[m]
θ	Pitch angle	[°]
θ_p	Degree of propeller plane	[°]
θ_{pn}	The angle of fore body	[°]
Λ	Aspect ratio	[-]
μ	Viscosity	[Pa·s]
μ_t	Turbulent viscosity	[Pa·s]
ν	Kinematic viscosity	[m^2/s]
ρ	Density of phase	[kg/m^3]
ρ_a	Density of air phase in a cell	[kg/m^3]
ρ_w	Density of water phase in a cell	[kg/m^3]
σ_ε	Equation Constant	[-]
σ_k	Equation Constant	[-]
τ_{ij}	Shear stress tensor	[kg/m·s^2]
ϕ_{pn}	The angle of aft body	[°]
ϕ^∞	Grid independent solution of ϕ^n	[-]
ϕ^n	Solution of ϕ in nth grid	[-]
ϕ^{n-1}	Solution of ϕ in $n-1$th grid	[-]
ω_n	Nominal wake	[-]

List of Figures

doi:10.6342/NTU202304123

doi:10.6342/NTU202304123

List of Tables

doi:10.6342/NTU202304123

Chapter 1 Introduction

1.1 Motivation

Taiwan has been continuously developing onshore wind farms for many years. Because Taiwan is surrounded by sea with dense mountains and few plains, offshore wind farms are considered to be a more suitable energy option. With the development of offshore wind farms, the demand for crew transportation between harbors and wind turbines continues to increase [1]. Crew transfer vessels (CTV) play a crucial role in transporting personnel and supplies in the operation and maintenance (O&M) of wind turbines. Optimizing the resistance of these vessels ensures efficient operations, and extends operational hours. Among them, small water-plane area twin hull (SWATH) vessels are particularly popular for this purpose due to their excellent seakeeping performance. However, SWATH vessels also face a primary challenge: Despite an excellent seakeeping performance, the small wave-induced force can lead to a lack of longitudinal stability [2].

For SWATH vessels, pontoon resistance dominates the total resistance of ship. The pressure distribution governed by the shape of the pontoon generates the Munk moment, leading to longitudinal instability of SWATH vessels. Therefore, optimizing the pontoon design can simultaneously improve the resistance performance and longitudinal stability in SWATH vessels. Currently, several studies have analyzed the pontoon resistance using numerical predictions, but effective design methods are not available [3-5]. Furthermore, to overcome the longitudinal instability of SWATH vessels, they are generally equipped with fin stabilizers to provide lift to balance Munk moments, especially at high speeds. However, increasing longitudinal stability also contributes to the total resistance [6], making the location of fin stabilizers a critical issue in the design process.

doi:10.6342/NTU202304123

Currently, computational fluid dynamics (CFD) software [7] has become an effective tool for designing and analyzing ship performance, offering significant advantages over ship model experiments. However, predicting ship resistance considering the free surface effect still takes relatively high computational cost, motivating the development of a more simplified approach. In addition to simplifying computational methods, this study utilizes artificial intelligence techniques, particularly deep neural networks (DNN), to aid in the design optimization. DNN, as a branch of artificial intelligence, can effectively model the nonlinear correlation between hull form and resistance, enabling the identification of optimal design parameters within a defined range. Although there have been numerous studies applying neural networks to SWATH hull optimization [8, 9], no research focuses on a parameterized hull form design optimization for total resistance reduction. Hence, the main objective of this study is to propose a DNN model to address this research gap.

doi:10.6342/NTU202304123

1.2 Literature Review

1.2.1 SWATH Vessel Design

The concept of a SWATH vessel has been developed since 1970s. There have been several successful applications of SWATH vessels, including oceanographic research vessels such as National Oceanic and Atmospheric Administration (NOAA) Ferdinand R. Hassler [10], offshore patrol vessels [11], navy vessels, such as the sea shadow [12]. Figure 1 and Figure 2 show the applications of SWATH.

There are two significant components of SWATH vessels. One is the pontoon immersing below the free surface and providing the major buoyancy of SWATH; another one is the strut piercing the free surface and connecting the deck and pontoon.

SWATH vessels are known for good seakeeping performance in high sea states compared with other categories of ship [13]. There are several advantages of SWATH vessels such as low resistance at high speed, small wave-induced forces, and large deck area. Despite these advantages, SWATH vessels still have some drawbacks such as increased shear resistance due to a sizeable wetted surface of the pontoon, especially for low speed, the lack of longitudinal restoring force due to a small water-plane area on the strut, the Munk moment of the pontoon, and the complexity arising from the fin stabilizer installed on hull surface [14-16]. As the pontoon is the main contributor of the instability [17-19] and dominates the resistance of SWATH vessels, this study focuses on optimizing the hull form of the underwater pontoon.

doi:10.6342/NTU202304123

1.2.2 Deep Neural Networks

Statistical analysis drawing insights from existing ships has been employed in the traditional approach of hull form optimization to establish the correlation between hydrodynamic performance and the geometric parameters of hull form. [20, 21]. However, statistical analysis approaches like linear regression may face challenges when the dependence of the target function on the parameters is not explicitly available. Consequently, novel methods such as neural networks, are required to optimize the hull form.

Neural networks have been widely applied to the field of naval architecture with significant success. In hull form resistance optimization, [22] and [23] employed free-form deformation techniques, while [24] utilized principal component analysis (PCA) to reduce the dimensionality of ship form parameters. These reduced parameters are then used as inputs of DNN to predict the resistance of various hull forms in the ship resistance optimization. In another study [25], the flow field pressure distribution, free surface elevation, and wake images of different hull forms were utilized as inputs to train a convolutional neural network (CNN) model, which predicts the hydrodynamic performance and resistance of different ship hulls. Similarly, neural networks have been successfully applied to consider sea conditions and ship motions. [26] and [27] trained neural networks using descriptors of sea condition parameters and wave characteristics to predict short-term future sea conditions and wave states. [28] employed hull form parameters to train neural networks for predicting the seakeeping performance of ships. Furthermore, [29] and [30] trained neural networks to predict short-term ship motions. Neural networks have also found applications in ship structural analysis. [31] and [32] utilized neural networks to predict the ultimate strength and fatigue failure of ship transverse structures. In the context of engine power prediction, [33] and [34] respectively

doi:10.6342/NTU202304123

employed the hull form information and ocean environmental data, along with ship speed, to train neural networks for predicting the required engine power. Moreover, [35] predicted the fuel consumption using information about the engine, propulsion system, flow field, and cargo load. Finally, [36] utilized publicly available data of ship and engine performance, as well as meteorological data, to predict the energy efficiency operational indicator (EEOI).

There are many kinds of models of neural networks, such as Recurrent Neural Networks (RNN), Long Short-Term Memory (LSTM), CNN, and DNN. DNN is a classic feed-forward network. In DNN, data flows directly from the input layer to the output layer without any backward flow. Because the hull form design parameters in this study are neither sequential nor two-dimension data, that means DNN is suitable for this study.

doi:10.6342/NTU202304123

Figure 1 Ferdinand R. Hassler [10]

Figure 2 Sea Shadow [12]

doi:10.6342/NTU202304123

1.3 Framework

In this study, the optimization process of pontoon design is briefly described. The first part is the resistance component analysis of the SWATH vessel. This study linearizes the total resistance as the resistance sum of the main components of the SWATH. The second part is a parametric pontoon design using Grasshopper3D. In this part, the pontoon is defined by these parameters. After the shape of the pontoons is defined by design parameters, the resistance analysis of the pontoon, strut, and fin stabilizer using the CFD software STAR-CCM+ is independently performed. As soon as the resistance of SWATH is obtained, the result is used to train the DNN model. Then, the DNN model is used to predict the optimized design parameters. Finally, the total resistance of the optimized SWATH vessel is validated by the CFD tool STAR-CCM+. Figure 3 shows the framework of the design optimization of the pontoon.

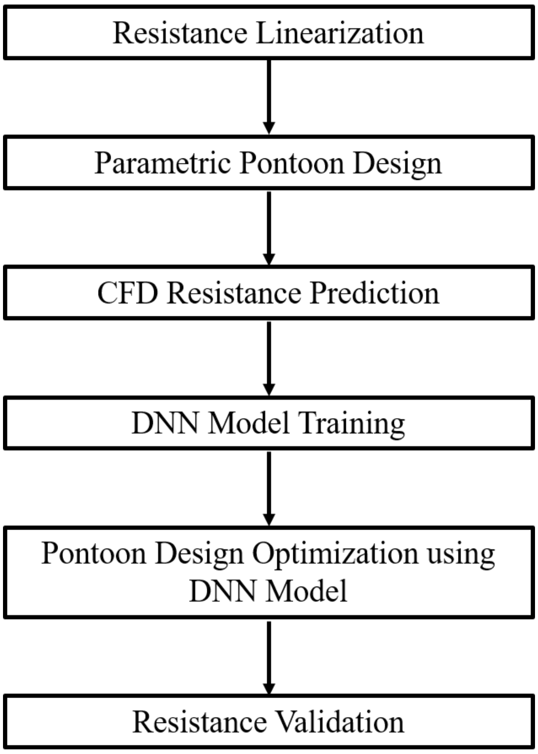

Figure 3 The Optimization Process of Pontoon Design

Chapter 2 Parametric Design of SWATH Vessel

2.1 Principle Dimension of Baseline Design

The baseline design of a SWATH vessel is provided by a shipyard. The displacement of the baseline design is 120 tons, with the longitudinal center of buoyancy (LCB) located at 12.88 meters. Figure 4 shows the different views and definitions of the hull form, where L_{OA} is length overall, L_{WL} is waterline length, D is ship depth, L_{pn} is pontoon length and B_{OA} is beam overall. Table 1 shows the principal dimensions of the SWATH vessel.

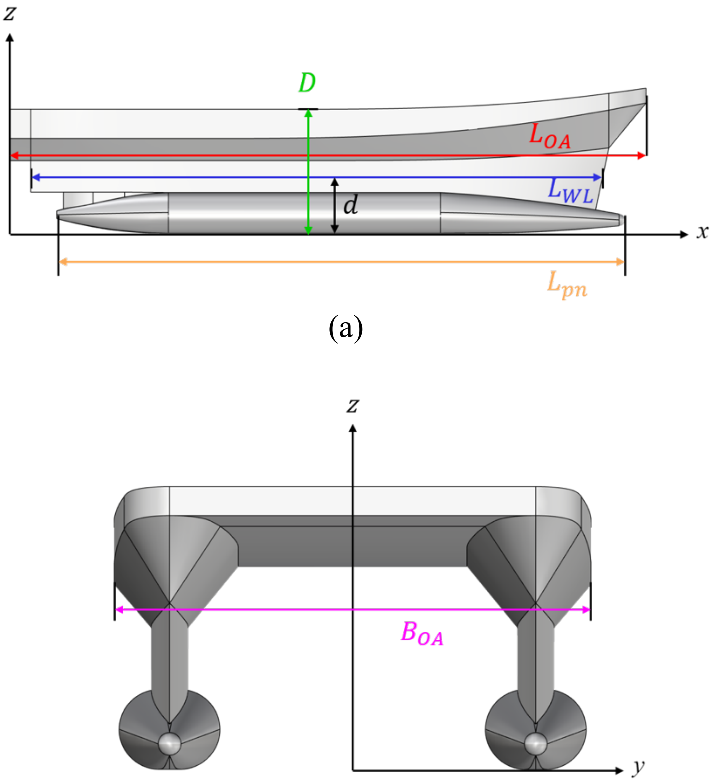

(a)

(b)

Figure 4 Baseline SWATH Vessel: (a) *x*-*z* Plane, (b) *y*-*z* Plane

Table 1 Principal Dimensions of Baseline SWATH Vessel

L_{OA} (m)	B_{OA} (m)	D (m)	L_{WL} (m)	L_{pn} (m)	d (m)	LCB (m)
26	9.8	5.0	23.4	23.2	2.18	12.88

doi:10.6342/NTU202304123

2.2 Geometric Modeling Tool

Rhinoceros 3D, a widely used computer-aided design software, is a freeform-based construction software [37]. Its Grasshopper3D module [38, 39] provides the ability of parametric design. Figure 5 shows the Grasshopper3D code and the corresponding Rhinoceros 3D workspace. In this figure, three points are used to define a curve segment. This study selects B-spline to construct the pontoon surface. After positions of seven points have been defined, four curves are automatically generated. The axisymmetric pontoons are obtained by rotating these curves along the central axis. This study utilizes Grasshopper3D to quickly parametrically create different pontoon geometries. The definition of the B-spline curve expresses as follows:

$$C(u) = \sum_{i=0}^{n} N_{i,p}(u) P_i. \tag{2.2.1}$$

As shown in Eq. (2.2.1), the B-spline curve is defined by a set of B-spline basis functions of degree p, denoted as $N_{i,p}(u)$. To construct a B-spline curve, the knot vector with $m + 1$ knots, the degree p, and the set of $n + 1$ control points are required. It is essential to satisfy the condition $m = n + p + 1$. More precisely, to define a B-spline curve of degree p with $n + 1$ control points, $n + p + 2$ knots, namely $u_0, u_1, \dots, u_{n+p+1}$, must be provided. Conversely, if a knot vector consisting of $m + 1$ knots and $n + 1$ control points is given, the degree of the B-spline curve can be determined as $p = m - n - 1$. These knot points partition the B-spline curve into segments, where each segment is defined by a specific knot span.

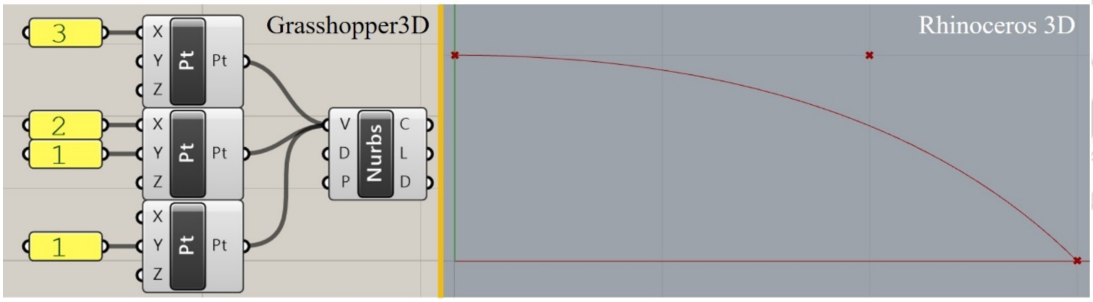

Figure 5 Schematic Illustration of Grasshopper 3D Code

2.3 Design Parameters of Pontoon

In this study, a parametric approach of pontoon design is proposed. The length of the pontoon (L_{pn}) is fixed to 22.5 m. The pontoon has four independent parameters and two dependent parameters, respectively. The independent ones are the length of the fore-body (L_f), the length of the aft-body (L_a), the angle of the fore-body (θ_{pn}), and the angle of the aft-body (ϕ_{pn}). The dependent ones are the length of the parallel middle body (L_m) which depends on L_f and L_a and is shown below:

$$L_m = L_{pn} - L_f - L_a, \tag{2.3.1}$$

and the radius of pontoon (R), which depends on L_f, L_a, θ_{pn}, and ϕ_{pn}, under the assumption of constant displacement. Figure 6 illustrates the design parameter of the pontoon, and Table 2 shows the ranges of each independent design parameter of the pontoon. L_f and L_a start from 1.8 m and increase by the interval size 1m to 7.8 m. θ_{pn} and ϕ_{pn} start from 10° and increase by the interval size 10° for each case to 60°. R_{hub} is the radius of the pontoon hub which is 0.15 m.

Figure 7 shows the control point arrangement to define the outline of the pontoon. Despite the third and fourth points, which are connected by a straight line, other points define two B-Spline segments. The first and third points define L_f, and the fourth and sixth points define L_a. The first and second points determine θ_{pn}, and the fourth and fifth points determine ϕ_{pn}. A total of 1398 pontoon models are generated for the resistance prediction.

doi:10.6342/NTU202304123

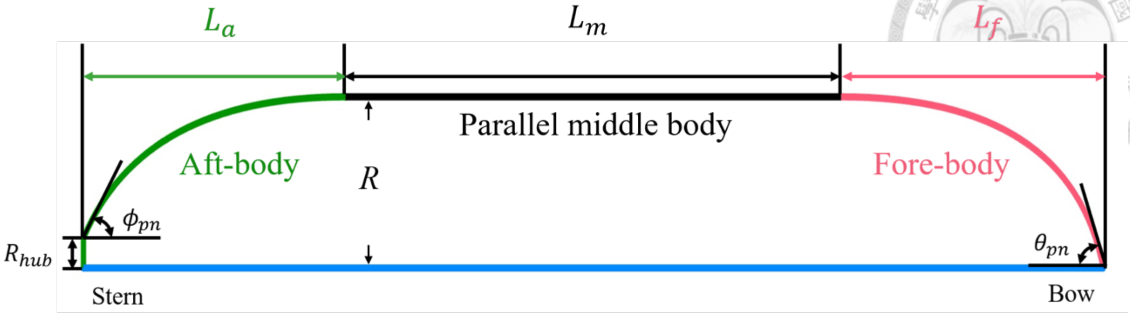

Figure 6 Design Parameters of Pontoon

Table 2 Design Parameter Range of Pontoon

Parameters	L_f (m)	L_a (m)	θ_{pn} (°)	ϕ_{pn} (°)
Ranges	1.8-7.8	1.8-7.8	10-60	10-60
Interval Size	1.0	1.0	10	10

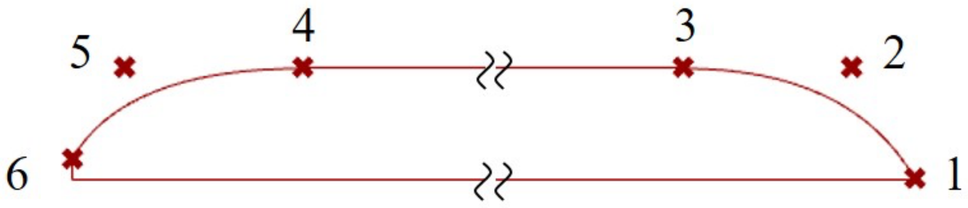

Figure 7 Control Point Arrangement to Define the Outline of Pontoon

2.4 Fin Stabilizer

Since SWATH vessels are prone to deliver sufficient longitudinal stability, the installation of fin stabilizers becomes necessary [40]. Figure 8 shows the fin stabilizer arrangement on the baseline design. The fore fin stabilizer is located 21.04 m from the stern, and the aft fin stabilizer is located 10.06 m from the stern. Figure 9 shows the working mechanism of fin stabilizers, where M_{fin} is the moment produced by the fin stabilizer to balance the Munk moment. The baseline design is equipped with a control system that only drives the fore stabilizer. During navigation, only the fore stabilizer is an active device, while the aft stabilizer is always parallel to the still water line. Figure 10 and Figure 11 show the dimensions and the different views of fin stabilizers with the dimensions marked in the figure. The aft and fore fin stabilizers are built with symmetrical foil sections, NACA0015 and NACA0030, respectively. The aspect ratios of aft and fore fin stabilizers are 0.668 and 0.689, respectively. Figure 12 shows the lift and drag coefficient (C_L and C_D) of the fin stabilizer, where the slope of the ideal lift in 2D is 2π [41]. The lift coefficient can be approximated by the following empirical equation proposed by *Söding*:[42]

$$C_L = \frac{2\pi\Lambda(\Lambda + 1)}{(\Lambda + 2)^2}\sin\alpha + C_q \sin\alpha\,|\sin\alpha|\cos\alpha, \qquad (2.4.1)$$

where Λ is the aspect ratio, $C_q = 1.0$ is used for hydrofoils with a sharp upper and lower edge.

The fin stabilizer provides lift force that keeps the ship without trim. However, the lift force is accompanied by the drag force. Figure 12 shows the drag force grows with the increase of the angle of attack. If the ship trim angle is too large, it may cause a large angle of attack of the fin stabilizer to balance the moment, where a large total resistance is expected.

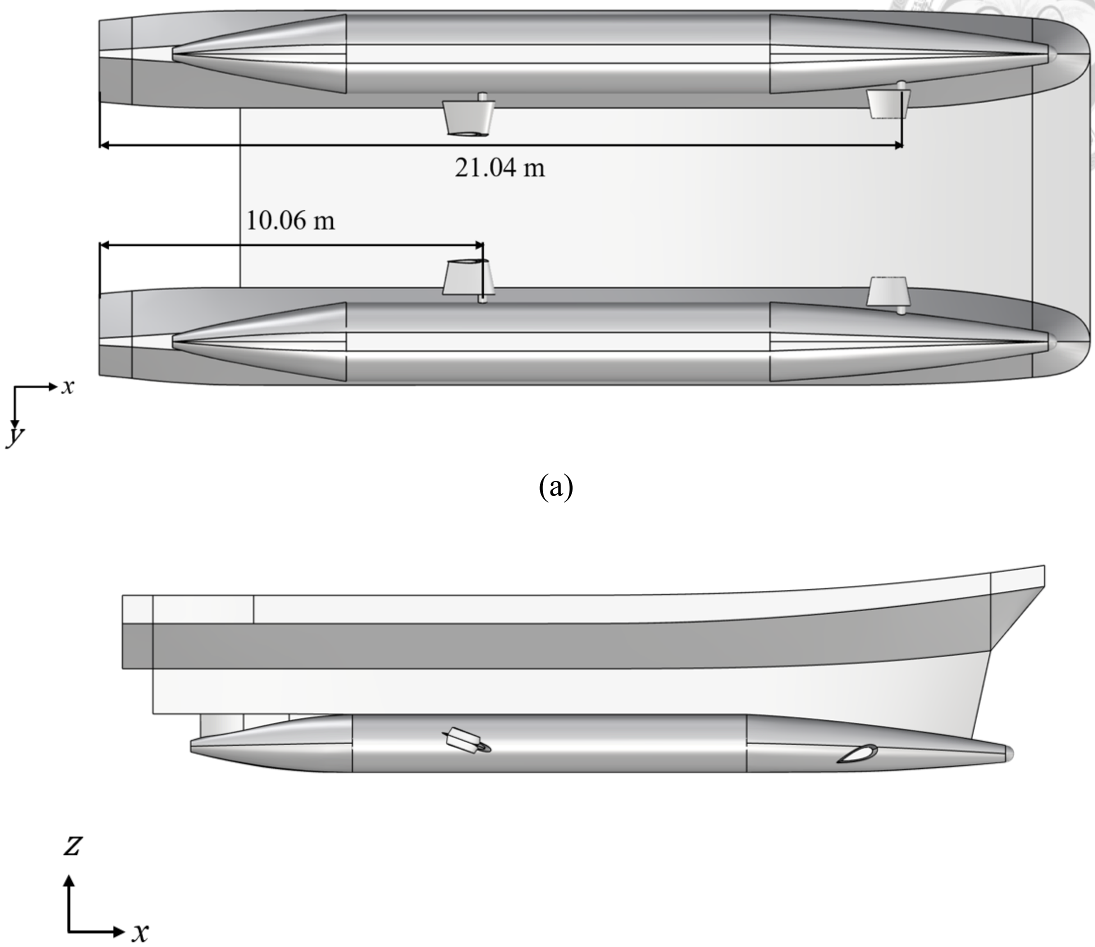

(a)

(b)

Figure 8 Baseline SWATH Vessel with Fin Stabilizer: (a) Bottom View, (b) Side View

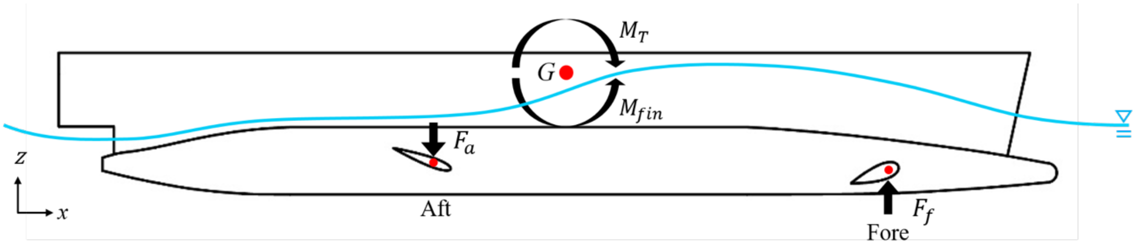

Figure 9 Working Principal of Fin Stabilizer

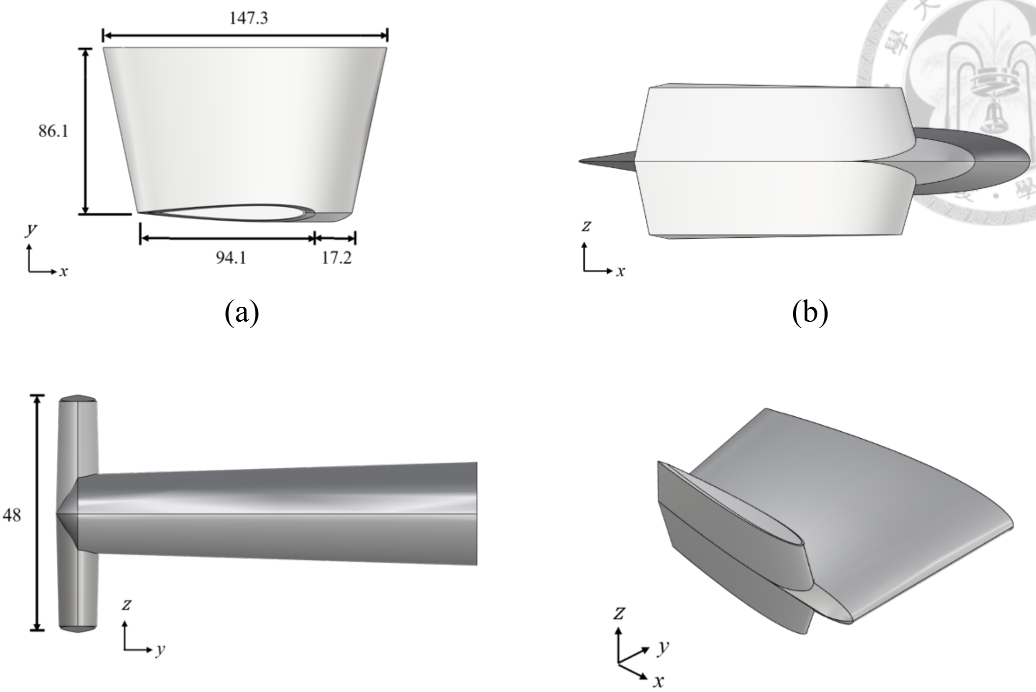

(a) (b)

(c) (d)

Figure 10 Aft Fin Stabilizer (cm): (a) Top View, (b) Side View, (c) Front View, (d) Perspective View

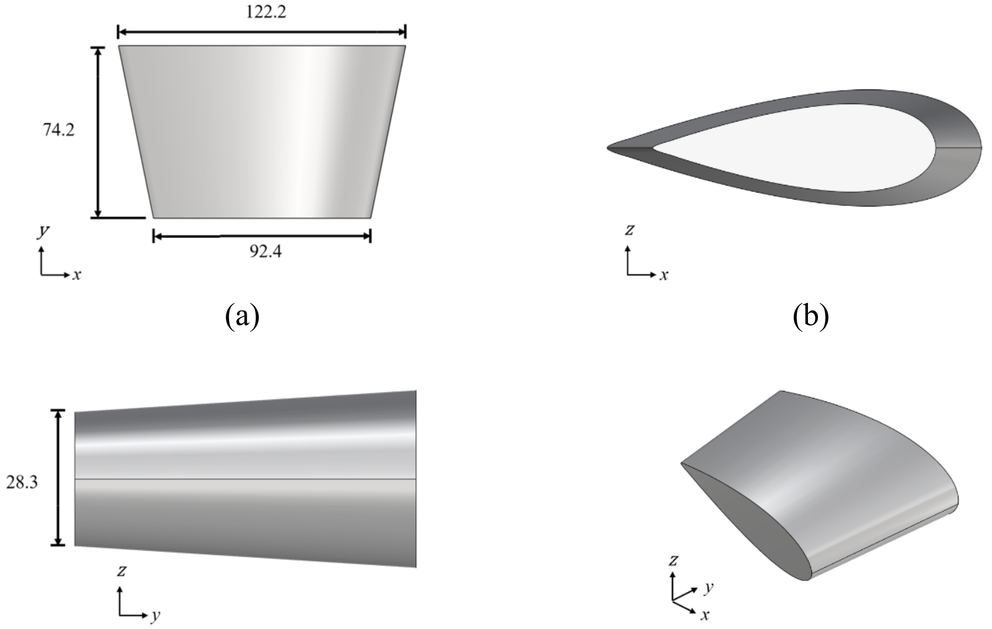

(a) (b)

(c) (d)

Figure 11 Fore Fin Stabilizer (cm): (a) Top View, (b) Side View, (c) Front View, (d) Perspective View

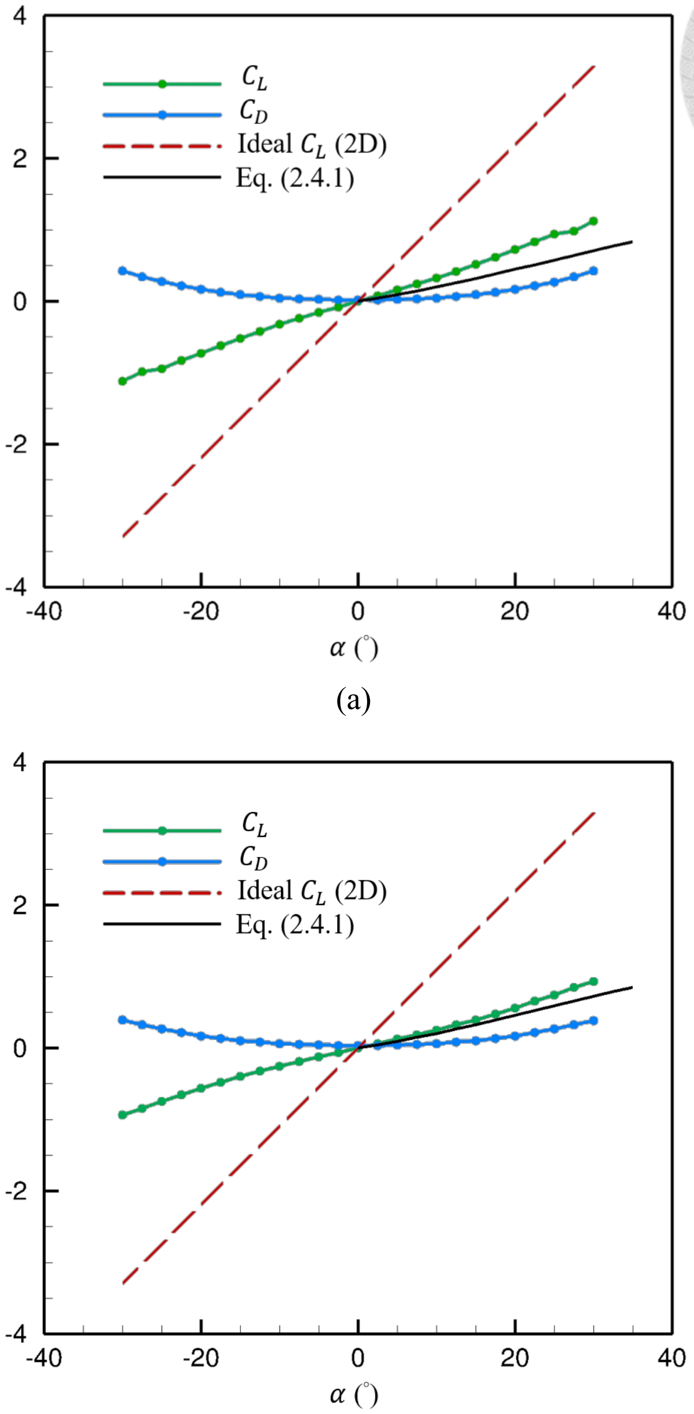

(a)

(b)

Figure 12 Lift and Drag Coefficient: (a) NACA0015, (b) NACA0030

Chapter 3 Resistance Linearization of SWATH

In order to avoid excessive computational efforts when considering the free surface effect in the CFD computation, this study decouples the SWATH resistance via a simplified approach. Table 3 shows the resistance of SWATH before and after decoupling. According to Table 3, the total resistance of SWATH can express as follows:

$$R_T = R_{st}(Fr) + R_L(Re, d), \tag{3.1}$$

where R_T is the total resistance of SWATH, $R_{st}(Fr)$ is the strut resistance, and $R_L(Re, d)$ is the resistance of the lower hull. R_{st} is mainly a function of the Froude number, and R_L is a function of the Reynolds numbers and draught. Moreover, the resistance of the lower hull R_L can be further expressed as follows:

$$R_L = R_{pn}(Re, d) + R_{fin}(Re, \alpha, d), \tag{3.2}$$

where R_{pn} is the resistance of the pontoon, and R_{fin} is the resistance of the fin stabilizer, which changes with the angle of attack α and the draught d. In Table 3, the decoupled resistance of the fin stabilizer is obtained from a fully submerged flow field. Since the difference between coupled and decoupled is small for fin stabilizers, it justifies the adaptation of a decoupled approach. Because the dimension of the fin stabilizer is relatively small compared to the draught, the impact of draught d is not significant for fin stabilizers. Figure 13 shows the pressure and shear resistance of the pontoon, R_{pn}^p and R_{pn}^s, change with the draught d. The correction β represents the ratio of pontoon resistance R_{pn}, at the draught d, to the pontoon resistance in the fully submerged case R_{pn}^{∞}. R_{pn} is then obtained by multiplying fully submerged pressure resistance $R_{pn,p}^{\infty}$ with β and then adding to the fully submerged shear resistance $R_{pn,s}^{\infty}$. R_{pn}^p drops rapidly with draught, but R_{pn}^s is nearly constant when the draught goes deeper. Finally, the resistance of the pontoon can be expressed as follows:

doi:10.6342/NTU202304123

$$R_T = R_{st}(Fr) + R_{pn,p}^{\infty}(Re) \cdot \beta\left(d_{pn}\right) + R_{pn,s}^{\infty}(Re) + R_{fin}(Re, \alpha), \tag{3.3}$$

where $\beta(d_{pn})$ is the correction of the draught effect, and d_{pn} defines in Figure 14. β is defined in the following equation:

$$\beta = \frac{R_{pn}^{p}}{R_{pn,p}^{\infty}} \tag{3.4}$$

The fin stabilizers provide lift force (L_{fin}) and the drag force (R_{fin}), both are functions of the angle of attack (α). The lift force is used to balance the Munk moment of the hull, M_T, which can be expressed as follows:

$$M_T = M_{pn}^{\infty} + M_{st}^{fs} = L_G \cdot F_{sta}, \tag{3.5}$$

$$F_{sta} = F_f + F_a, \tag{3.6}$$

where M_{st}^{fs} is the moment of the strut, F_{sta} is the force of fin stabilizer, F_f and F_a are respectively the lift force produced by the fore fin and the aft fin, fs means the free surface flow. M_{pn}^{∞} can be further expressed as follows:

$$M_{pn}^{\infty} = M_{pn,s}^{\infty} + M_{pn,p}^{\infty}, \tag{3.7}$$

$$M_{pn,p}^{\infty} = \sum_{i} p_{pn,i}^{\infty} \cdot A_{pn,i}^{\infty} \cdot L_{G,i}, \tag{3.8}$$

$$M_{pn,s}^{\infty} = \sum_{i} s_{pn,i}^{\infty} \cdot A_{pn,i}^{\infty} \cdot L_{G,i} \tag{3.9}$$

where p_{pn}^{∞} is the pressure of the pontoon, s_{pn}^{∞} is the shear stress of the pontoon, A_{pn}^{∞} is the surface area of the pontoon, and L_G is the length of the lever arm from the center of gravity. $M_{pn,p}^{\infty}$ is the moment caused by the pressure on the pontoon, while $M_{pn,s}^{\infty}$ is the moment caused by the shear stress on the pontoon. The superscript, ∞, means the fully submerged flow field.

Figure 15 shows the pressure distribution on the pontoon. The blue dot represents the free surface elevation. As the figure shows, the free surface influence on the pressure distribution is small, so this study uses the pontoon moment in a fully submerged flow field as an approximation of the Munk moment.

Due to the aforementioned resistance decoupling, the resistance of individual components of the SWATH vessel is calculated under different flow conditions. The fin stabilizer resistance is calculated under a fully submerged flow assumption, the pontoon resistance is calculated under a fully submerged flow assumption, and the strut resistance is predicted under a free surface flow assumption.

Table 3 The Resistance Components of SWATH

Part	Coupled (kN)	Decoupled (kN)	Difference (%)
Strut	24.9	22.9	-8.2
Pontoon	69.6	66.6	-4.4
Fore Fin	16.5	17.4	4.9
Aft Fin	7.5	7.8	3.5
Total	118.7	114.8	-3.2

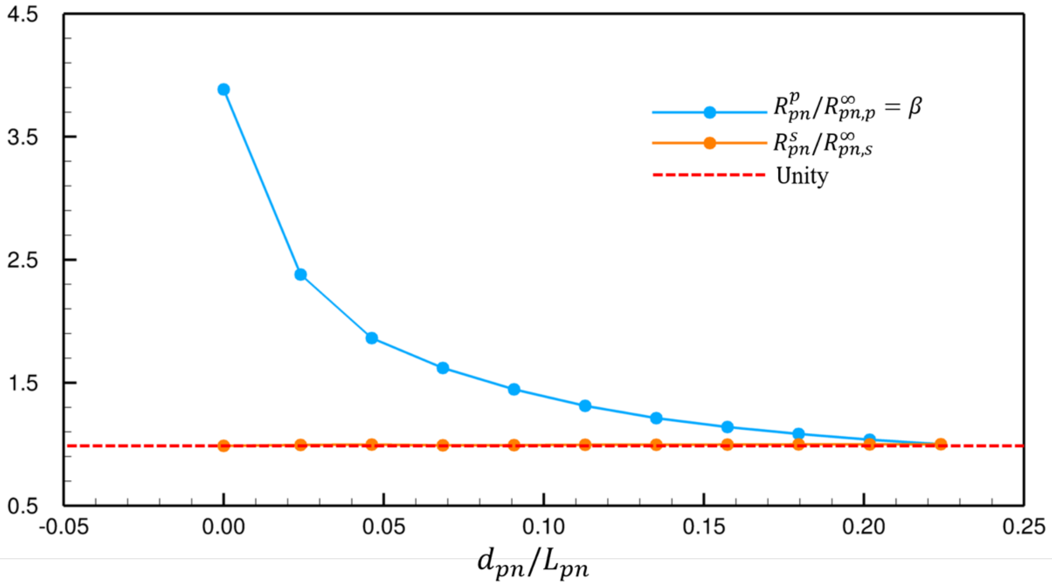

Figure 13 Pontoon Resistance vs. Draught

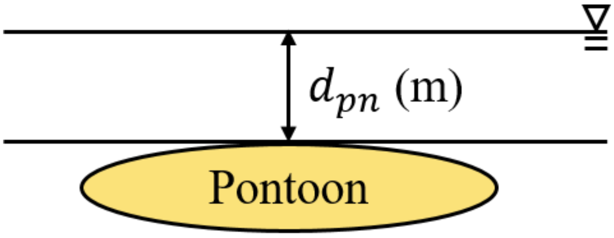

Figure 14 Draught of Pontoon

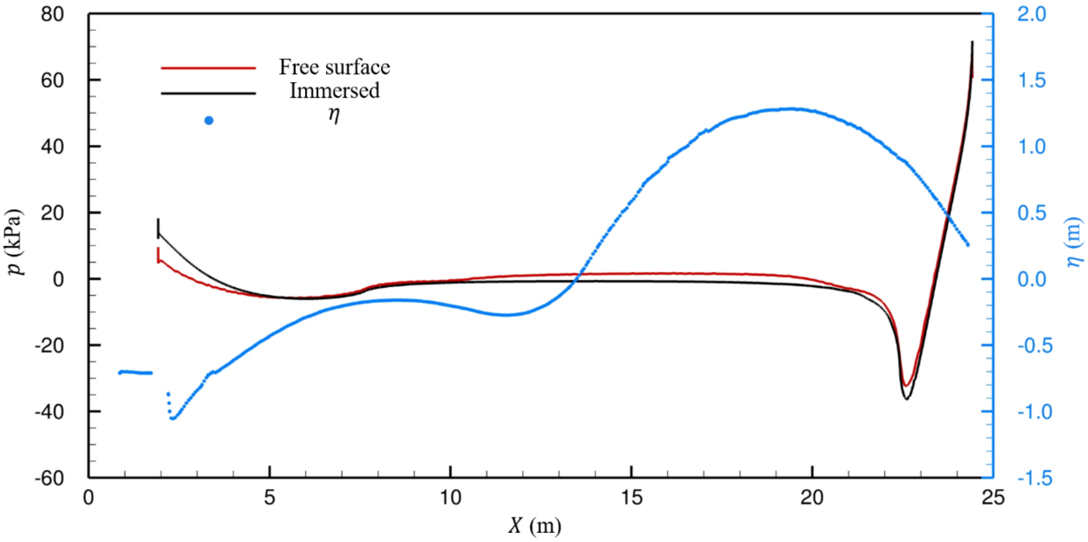

Figure 15 Comparison of Surface Pressure on Pontoon between Two Conditions

doi:10.6342/NTU202304123

Chapter 4 Flow Model

In this study, the resistance of the SWATH vessel is simulated using the commercial software STAR-CCM+, based on the finite volume method (FVM). STAR-CCM+ iteratively solves the governing equations, including the continuity equation and the Reynolds-Averaged Navier-Stokes (RANS) equation, and applies the turbulence model to predict the ship resistance and the corresponding flow field. The simulations for the pontoon under fully submerged conditions are assumed axisymmetric, while the full-scale SWATH vessel considering the free surface is simulated in a three-dimensional flow field. Figure 16 shows the coordinate system of the axisymmetric and three-dimensional flow fields. Additionally, in an axisymmetric flow calculation, the z-axis is aligned with the longitudinal direction of the ship, while in the three-dimensional flow calculation, the x-axis represents the longitudinal direction, with the origin located at the stern and the positive direction extending towards the bow.

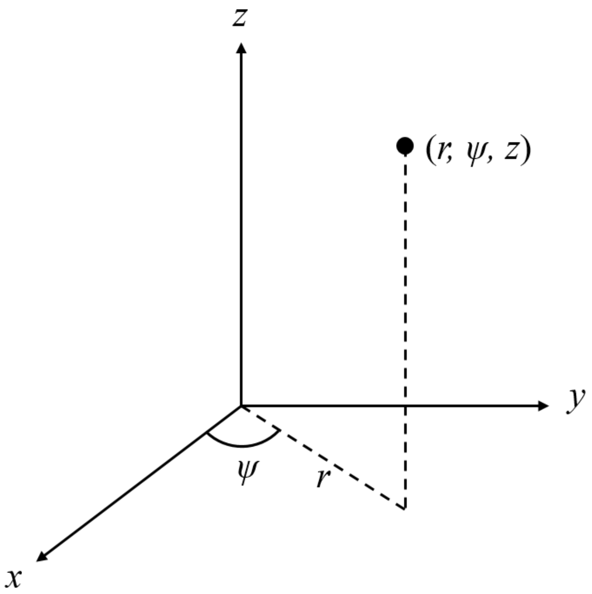

Figure 16 Coordinate System of Axisymmetric and Three-Dimensional Flow Region

doi:10.6342/NTU202304123

4.1 Governing Equations

4.1.1 Axisymmetric Pontoon Flow

The immersed cases are under an axisymmetric and steady flow assumption. The governing equations consist of continuity and momentum equations, and a $K-\varepsilon$ turbulence model is used to consider the turbulent effects. The equations are shown as follows:

(a) Continuity Equation

$$\frac{\partial(\rho u)}{\partial z}+\frac{1}{r}\frac{\partial(\rho r v)}{\partial r}=0, \tag{4.1.1}$$

(b) Momentum Equations

$$\frac{\partial(\rho u u)}{\partial z}+\frac{1}{r}\frac{\partial(\rho r u v)}{\partial r}=-\frac{\partial p}{\partial z}+\frac{\partial \tau_{zz}}{\partial z}+\frac{1}{r}\frac{\partial(r\tau_{zr})}{\partial r}, \tag{4.1.2}$$

$$\frac{\partial(\rho u v)}{\partial z}+\frac{1}{r}\frac{\partial(\rho r v v)}{\partial r}=-\frac{\partial p}{\partial r}+\frac{\partial \tau_{rz}}{\partial z}+\frac{1}{r}\frac{\partial(r\tau_{rr})}{\partial r}, \tag{4.1.3}$$

where (4.1.2) is for the axial direction, and (4.1.3) is for the radial direction. The stress tensor components are expressed as follows:

$$\tau_{zz}=2\mu\left(\frac{\partial u}{\partial z}-\frac{2}{3}\left(\frac{\partial u}{\partial z}+\frac{1}{r}\frac{\partial(rv)}{\partial r}\right)\right), \tag{4.1.4}$$

$$\tau_{rr}=2\mu\left(\frac{\partial v}{\partial r}-\frac{2}{3}\left(\frac{\partial u}{\partial z}+\frac{1}{r}\frac{\partial(rv)}{\partial r}\right)\right), \tag{4.1.5}$$

$$\tau_{rz}=\tau_{zr}=\mu\left(\frac{\partial u}{\partial r}+\frac{\partial v}{\partial z}\right), \tag{4.1.6}$$

(c) $K-\varepsilon$ Turbulence Model

The adopted turbulence model uses two transport equations to express the turbulence kinetic energy K and the dissipation rate ε as follows:

doi:10.6342/NTU202304123

$$\frac{\partial(\rho u K)}{\partial z}+\frac{\partial(\rho v K)}{\partial r}=$$

$$G-\rho\varepsilon+\frac{\partial}{\partial z}\left[\left(\mu+\frac{\mu_t}{\sigma_k}\right)\frac{\partial K}{\partial z}\right]+\frac{1}{r}\frac{\partial}{\partial r}\left[r\left(\mu+\frac{\mu_t}{\sigma_k}\right)\frac{\partial K}{\partial r}\right], \tag{4.1.7}$$

$$\frac{\partial(\rho u \varepsilon)}{\partial z}+\frac{\partial(\rho v \varepsilon)}{\partial r}=$$

$$c_{\varepsilon 1}G\frac{\varepsilon}{K}-c_{\varepsilon 2}G\frac{\varepsilon^2}{K}+\frac{\partial}{\partial z}\left[\left(\mu+\frac{\mu_t}{\sigma_\varepsilon}\right)\frac{\partial \varepsilon}{\partial z}\right]+\frac{1}{r}\frac{\partial}{\partial r}\left[r\left(\mu+\frac{\mu_t}{\sigma_\varepsilon}\right)\frac{\partial \varepsilon}{\partial r}\right], \tag{4.1.8}$$

$$G=\mu_t|\dot{\gamma}|^2, \tag{4.1.9}$$

$$|\dot{\gamma}|^2=$$

$$2\left(\frac{\partial u}{\partial z}\right)^2+2\left(\frac{\partial v}{\partial r}\right)^2+2\left(\frac{v}{r}\right)^2+\left(\frac{\partial v}{\partial z}+\frac{\partial u}{\partial r}\right)^2-\frac{2}{3}\left(\frac{1}{r}\frac{\partial}{\partial r}(rv)+\frac{\partial u}{\partial z}\right)^2, \tag{4.1.10}$$

$$\mu_t=c_\mu\rho\frac{K^2}{\varepsilon}, \tag{4.1.11}$$

where ρ is the density, u, v are the velocity components in the cylindrical coordinate system z, r, respectively, p is the pressure, μ is the viscosity, G is the production of turbulent kinetic energy, μ_t is the turbulent viscosity, and $\dot{\gamma}$ is the shear rate. The equation constants of the $K-\varepsilon$ turbulence model, $c_\mu, \sigma_K, c_{\varepsilon 1}, c_{\varepsilon 2}, \sigma_\varepsilon$, are shown in Table 4.

Table 4 Equation Constants for $K-\varepsilon$ Turbulence Model

c_μ	σ_K	$c_{\varepsilon 1}$	$c_{\varepsilon 2}$	σ_ε
0.09	1.00	1.44	1.92	1.30

4.1.2 Three-Dimension Free Surface Ship Flow

The governing equations for the simulation involving free surface are continuity and momentum equations, and the flow is assumed to be unsteady and incompressible. The governing equations are shown below:

(a) Continuity Equation

$$\frac{\partial U_i}{\partial x_i} = 0, \tag{4.1.12}$$

(b) Momentum Equations

$$\frac{\partial U_i}{\partial t} + \frac{\partial \left(U_i U_j\right)}{\partial x_j} = -\frac{1}{\rho}\frac{\partial p}{\partial x_i} + \frac{\partial}{\partial x_j}\left[\nu\left(\frac{\partial U_i}{\partial x_j} + \frac{\partial U_j}{\partial x_i}\right)\right] - \frac{\partial \overline{u_i' u_j'}}{\partial x_j}, \tag{4.1.13}$$

where U_i and u_i' are the mean and fluctuation velocity components in the direction of x_i, respectively, ν is the kinematic viscosity, and $\overline{\rho u_i' u_j'}$ is the Reynolds stress.

(c) $K-\varepsilon$ Turbulence Model

$$\frac{\partial K}{\partial t} + \frac{\partial \left(K U_j\right)}{\partial x_j} = \frac{\partial}{\partial x_j}\left[\left(\nu + \frac{\nu_t}{\sigma_k}\right)\frac{\partial K}{\partial x_j}\right] + \frac{1}{\rho}G_k - \varepsilon, \tag{4.1.14}$$

$$\frac{\partial \varepsilon}{\partial t} + \frac{\partial \left(K U_j\right)}{\partial x_j} = \frac{\partial}{\partial x_j}\left[\left(\nu + \frac{\nu_t}{\sigma_\varepsilon}\right)\frac{\partial \varepsilon}{\partial x_j}\right] + C_{\varepsilon 1} G_k \frac{\varepsilon}{\rho K} - C_{\varepsilon 2}\frac{\varepsilon^2}{K}, \tag{4.1.15}$$

where the equation constants of the equation are shown in Table 4. The turbulent kinematic viscosity ν_t is given as follows:

$$\nu_t = C_\mu \frac{K^2}{\varepsilon}, \tag{4.1.16}$$

where G_k is the turbulent production term expressed as:

$$G_k = -\rho\overline{u_i' u_j'}\frac{\partial U_i}{\partial x_j}, \tag{4.1.17}$$

and under the Boussinesq hypothesis, $-\rho_{sw}\overline{u_i' u_j'}$ can be expressed as follows:

$$-\rho\overline{u_i'u_j'} = \mu_t\left(\frac{\partial U_i}{\partial x_i} + \frac{\partial U_j}{\partial x_i}\right) - \frac{2}{3}\rho K\delta_{ij}, \tag{4.1.18}$$

where δ_{ij} is the unit tensor.

(d) Volume of Fluid Method

The volume of fluid method is employed to model free surface flows. The volume fraction of the fluid in a cell can be expressed as:

$$C_a = \frac{V_a}{V}, \tag{4.1.19}$$

$$C_w = \frac{V_w}{V}, \tag{4.1.20}$$

where V_a is the air volume in a cell, V_w is the water volume in a cell, and V is the total volume of a cell. The volume fraction of all fluids in a cell is equal to unity:

$$C_a + C_w = 1, \tag{4.1.21}$$

where $C_a = 0$ indicates that the cell does not contain air; $C_a = 1$ indicates the cell is fully occupied by air; $0 < C_a < 1$ indicates there is an interface in the cell. In this study, $C_a = 0.5$ is defined as the free surface location. The fluid density ρ and the fluid dynamic viscosity μ are calculated as follows:

$$\rho = \rho_a C_a + \rho_w C_w, \tag{4.1.22}$$

$$\mu = \mu_a C_a + \mu_w C_w, \tag{4.1.23}$$

where ρ_a and ρ_w represent the densities of air and water, respectively, and μ_a and μ_w represent the dynamic viscosities of air and water, respectively. The free surface equation is shown as below:

$$\frac{\partial C_a}{\partial t} + U_K\frac{\partial C_a}{\partial x_k} + \nabla\cdot\left(C_a U_{d,a}\right) + \nabla\cdot\left(C_a(1 - C_a)U_{c,a}\right) = 0, \tag{4.1.24}$$

where $U_{d,a}$ is the diffusion rate of air, and $U_{c,a}$ is the boundary sharpening speed of air.

$$U_{c,a} = C_\alpha |\mathbf{U}| \frac{\nabla C_a}{|\nabla C_a|}, \tag{4.1.25}$$

where C_α is the sharpening factor.

4.2 Computational Domain and Boundary Condition

This study defines different computational domains to solve the flow field around the pontoon in the fully submerged case and the free surface case.

4.2.1 Pontoon Flow

Figure 17 shows the computational domain in fully submerged conditions. Table 5 summarizes the dimensions of the domain geometry and the boundary conditions in a two-dimensional flow field. To ensure the resistances are independent of the domain size, different sizes of the computational domain are tested. Consequently, the inlet boundary is L_{pn} away from the fore-end and the outlet boundary is 2 L_{pn} away from the aft-end. The radius of the domain is L_{pn}. For the inlet boundary, the inlet velocity is the target vessel speed (V_s) of 24 knots, while pressure is set to 0 at the pressure outlet.

The simulation is conducted at $V_s = 24$ knots, and the corresponding Froude number (Fr) is 0.81, where Fr is defined by the vessel speed, waterline length (L_{WL}), and gravitational acceleration (g) as below:

$$Fr = \frac{V_s}{\sqrt{gL_{WL}}}. \tag{4.2.1}$$

doi:10.6342/NTU202304123

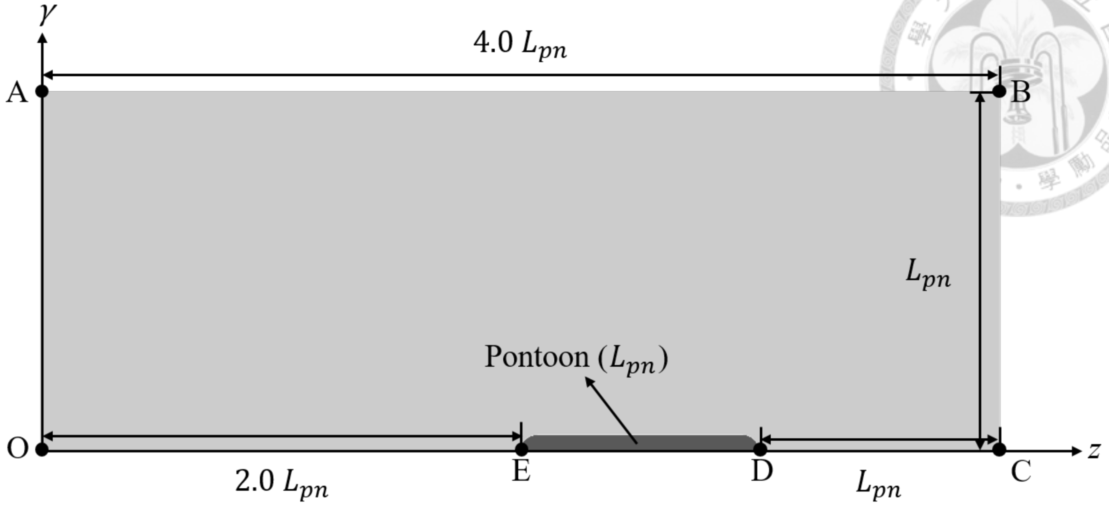

Figure 17 Schematic of the Computational Domain

Table 5 Dimension of the Computational Domain for Pontoon Flow

Region	Physical Definition	Boundary Condition
$\overline{\mathrm{AB}}$ (Top)	Inlet	$u = -V_s, v = 0$
$\overline{\mathrm{BC}}$ (Front)		
$\overline{\mathrm{OA}}$ (Back)	Pressure outlet	$p = 0$
$\overline{\mathrm{CD}}$ (Bottom)	Axis	$\frac{\partial u}{\partial \mathrm{n}} = 0, \frac{\partial v}{\partial \mathrm{n}} = 0$
$\overline{\mathrm{EO}}$ (Bottom)		
$\overline{\mathrm{DE}}$ (Pontoon)	Wall	$u = 0, v = 0$

4.2.2 Free Surface Ship Flow

Figure 18 illustrates the computational domain of the free surface case. The simulation only considers one-half of the ship to reduce the simulation time because the vessel is symmetric to $y = 0$. The front boundary is 1.5 L_{pn} away from the bow and the back boundary is 3.5 L_{pn} away from the stern. The port boundary is 1.5 L_{pn}, and the bottom boundary is 1.5 L_{pn} away from the hull. Table 6 summarizes the boundary conditions, where the inlet velocity is the target vessel speed of 24 knots, and for the pressure outlet boundary, the pressure is assumed hydrostatic pressure of calm water.

doi:10.6342/NTU202304123

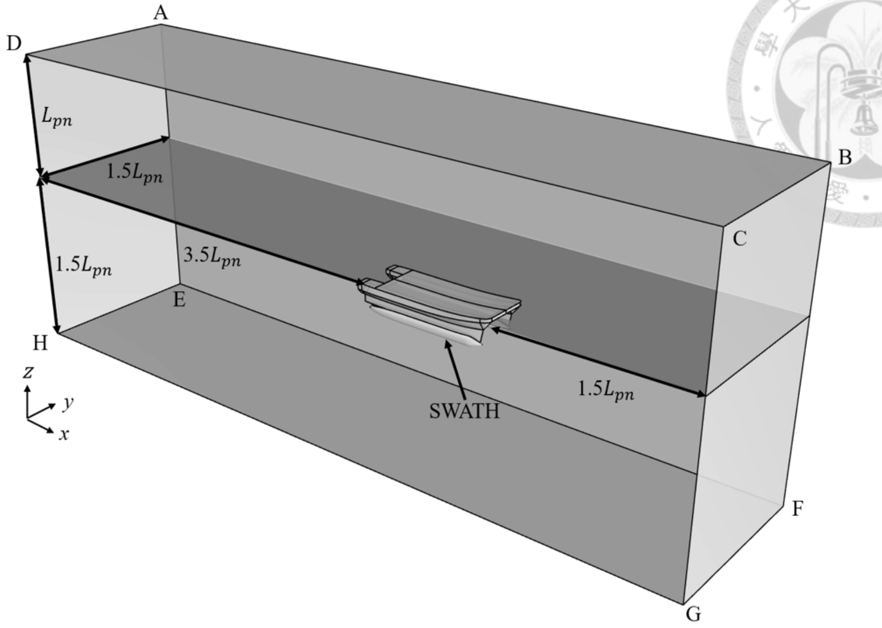

Figure 18 The Domain of Free Surface

Table 6 Dimension of Computational Domain of Free Surface

Region	Physical Definition	Boundary Condition
ABCD (Top)	Inlet	$\mathbf{U} = (-V_s, 0{,}0)$
BFGC (Front)		
ABFE (Port)		
EFGH (Bottom)		
AEDH (Back)	Pressure Outlet	$p = p_s(Z) = \rho g Z$
DCGH ($y = 0$)	Symmetry	$\frac{\partial \mathbf{U}}{\partial \mathrm{n}} = 0$
SWATH	Wall	$\mathbf{U} = 0$

4.3 Mesh Arrangement

4.3.1 Pontoon Flow

For fully submerged conditions, a 2D Cartesian mesh is used to discretize the computational domain. The base size of the background mesh is 1.4 m, which is 1/16 of the pontoon length, and the total cell number is approximately 250,000. Four boundary layers are used to capture the flow near the wall and transit to the background mesh.

Figure 19 shows the mesh arrangement of the whole domain, and Figure 20 shows the mesh near the pontoon. According to Figure 19, the mesh arrangement involves a finer mesh in the vicinity of the pontoon to accurately capture significant flow variations in that area. In contrast, a coarser mesh is utilized in the far-field region. Moreover, a finer surface mesh is employed on the surface of the pontoon to accurately capture the geometry feature, the pressure stress, and the shear stress, as shown in Figure 20.

doi:10.6342/NTU202304123

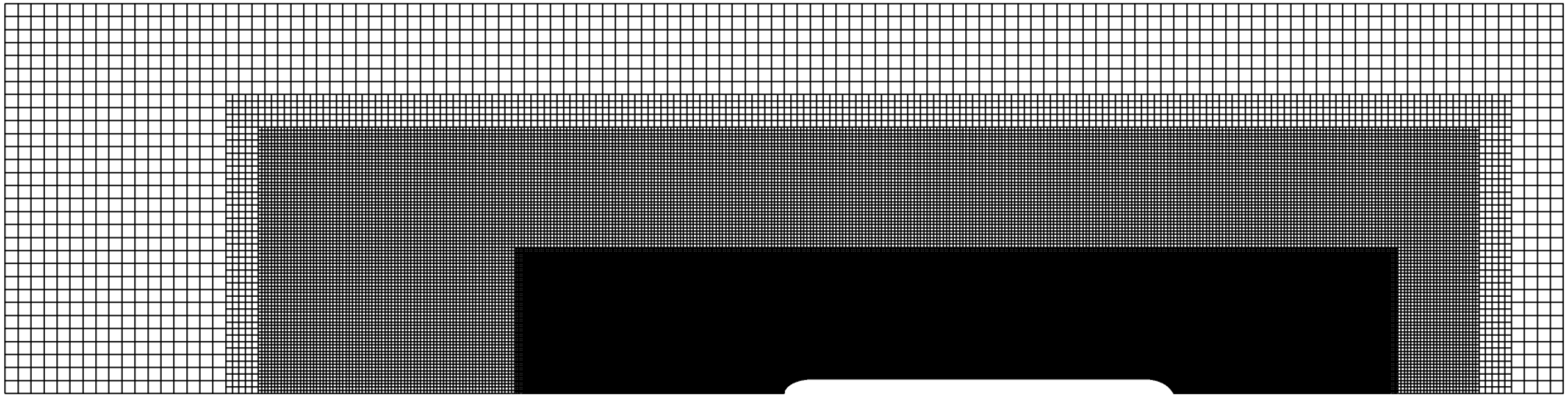

Figure 19 Mesh Arrangement of the Whole Domain

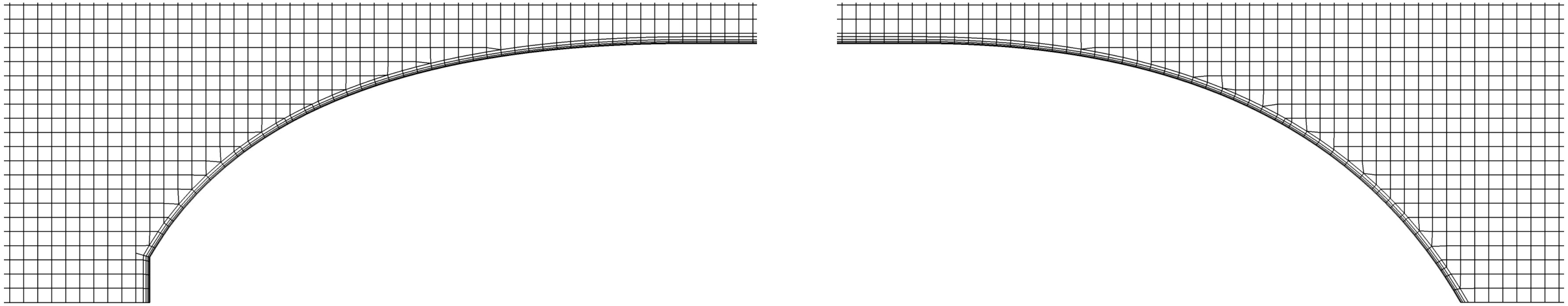

(a) (b)

Figure 20 Mesh near the Pontoon: (a) Aft Part, (b) Fore Part

doi:10.6342/NTU202304123

4.3.2 Free Surface Ship Flow

A three-dimensional Cartesian mesh is used to discretize the computational domain for free surface ship flows, where the base size of the mesh is 1 m. There are two boundary layers to capture flow near the wall and transit to the background mesh. The total cell number of the initial mesh is approximately 3 million. This study uses an adaptive mesh refinement (AMR) module of STAR-CCM+ to automatically track the free surface so that the refinement is only done in the right place to reduce the computational cost. With the AMR module, the total cell number of the final mesh becomes 6.15 million.

The AMR module utilizes the gradient of the volume fraction to identify the position of the free surface. Subsequently, it uses the transport equation to identify the location of the free surface for the next time step and accordingly adjusts the mesh through mesh refinement or coarsening. The AMR module ensures the mesh is not coarsened beyond its original level of refinement. As the AMR module does not alter the surface mesh density, the hull surface region needs to initially have a sufficient mesh density. Figure 21 illustrates the transition width and refinement layers of the free surface refinement used in the AMR module setting. Two refinement layers are employed to accurately capture the free surface. These layers consist of a specific number of grid layers that are gradually refined near the free surface region. The transition width refers to the number of grid layers used to smoothly transition from the refined layers to the background mesh, ensuring a smooth and accurate representation of the free surface. Figure 22 shows the initial mesh arrangement while Figure 23 shows the final mesh arrangement.

doi:10.6342/NTU202304123

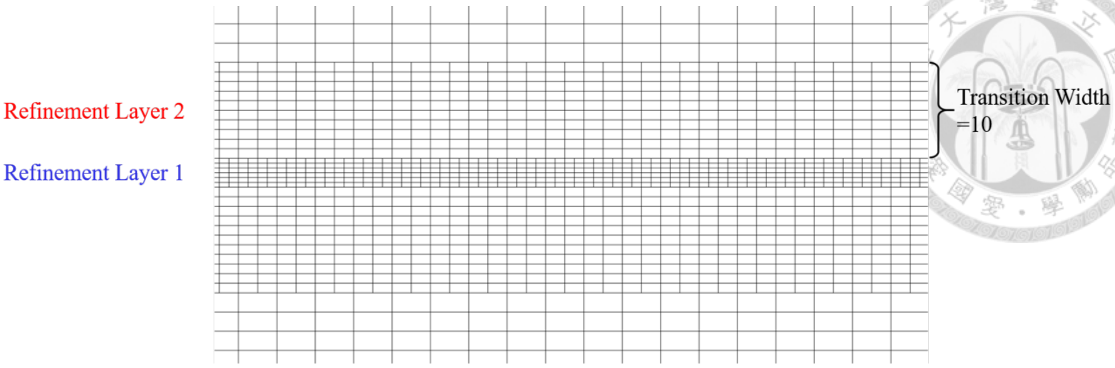

Figure 21 Transition Width and Refinement Layers

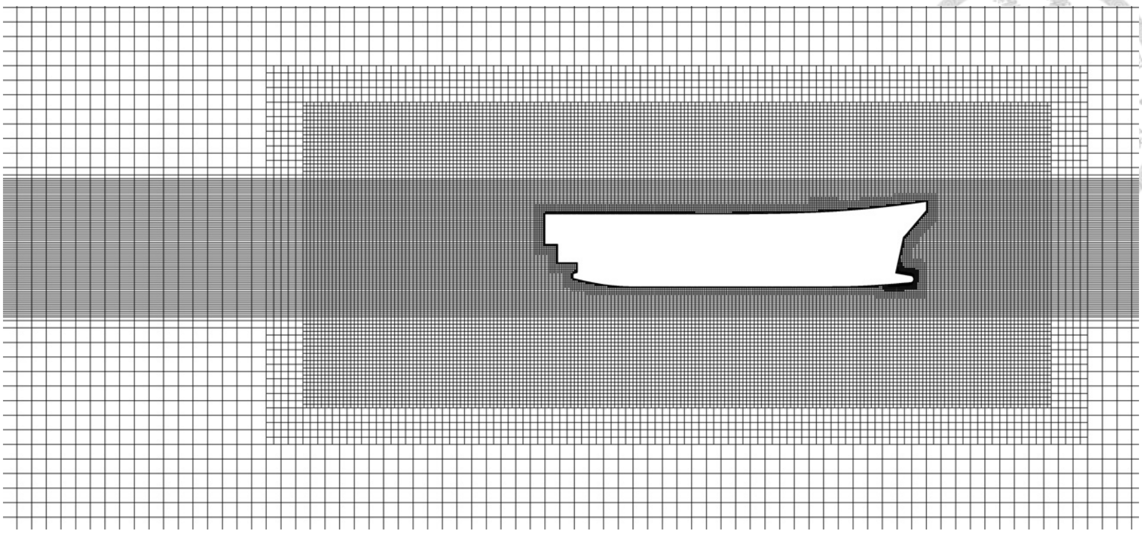
(a)

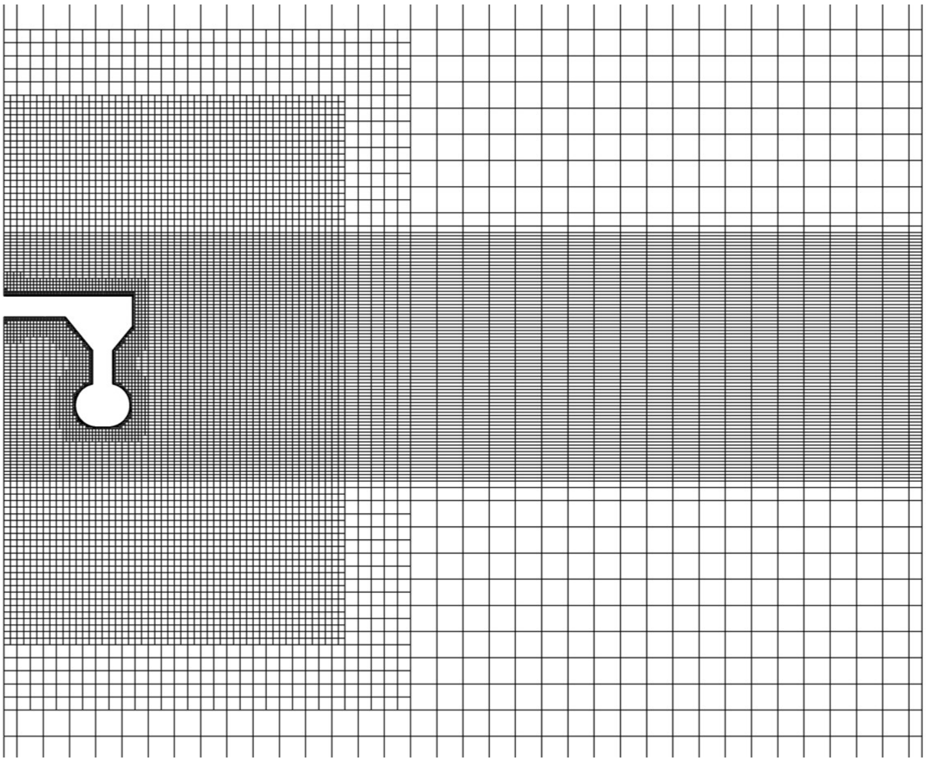
(b)

Figure 22 Initial Mesh Arrangement of Free Surface: (a) $y = 3.76$ m, (b) Midship

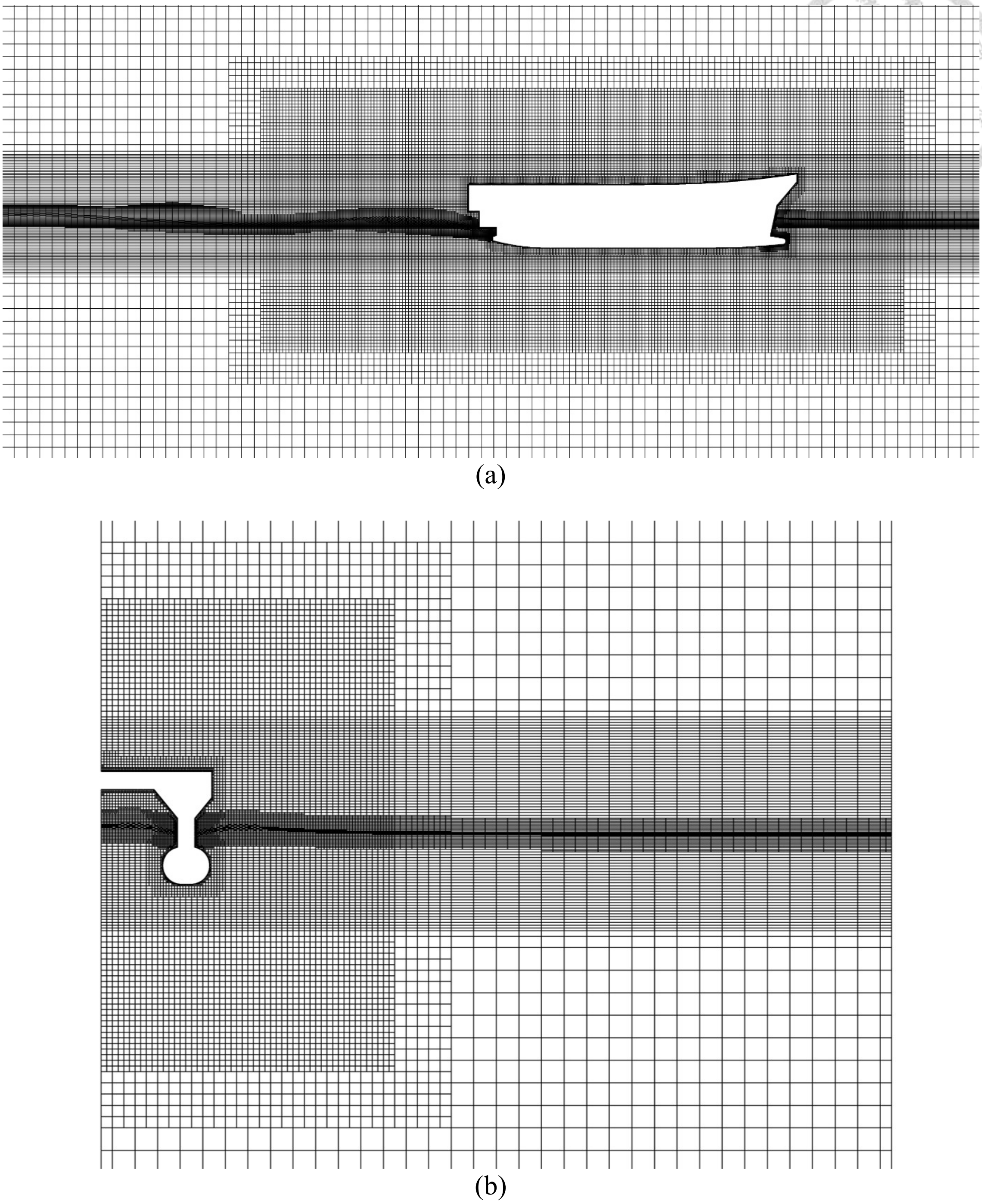

Figure 23 Mesh Arrangement of Free Surface after Simulation: (a) $y = 3.76$ m, (b) Midship

4.4 Grid Dependency

The number of grids in the computational domain is sensitive to the result in numerical simulation. A finer grid layout favorably leads to a better solution, but the growth of cell numbers clearly increases the simulation time. Therefore, a grid dependency analysis is used to illustrate the dependence of accuracy on grid number and choose a grid layout that can balance the accuracy and simulation cost.

The grid-independent solution ϕ^{∞} is calculated by second-order Richardson extrapolation as follows:

$$\phi^{\infty} = \phi^{n} + \frac{\phi^{n} - \phi^{n-1}}{\frac{N_n}{N_{n-1}} - 1} \tag{4.4.1}$$

where ϕ is the field variable, ϕ^{n} is the variable of the n-th grid level, and N_n is the number of cells of the n-th grid level. In this study, the resistance of the pontoon in the fully submerged flow field (R_{pn}^{∞}) is used to analyze the grid dependency. Table 7 shows the number of grids of five grid levels. Figure 24 shows the grid-independent solution, and Figure 25 shows the dependence of the discretization error E_{ϕ} on difference cell size dx, where E_{ϕ} and dx are expressed as follows:

$$E_{\phi} = \left| \frac{\phi^{\infty} - \phi^{n}}{\phi^{\infty}} \right|, \tag{4.4.2}$$

$$dx = \sqrt{\frac{1}{N}}. \tag{4.4.3}$$

As Figure 25 shows, the discretization error is close to that of an ideal second-order scheme. The cell number used in this study is grid level 3, where the discretization error is less than 3%.

doi:10.6342/NTU202304123

Table 7 Number of Cells and the Corresponding Resistance Prediction

Grid Level	1	2	3	4	5
R_{pn}^{∞}	20.8	20.3	19.9	19.7	19.5

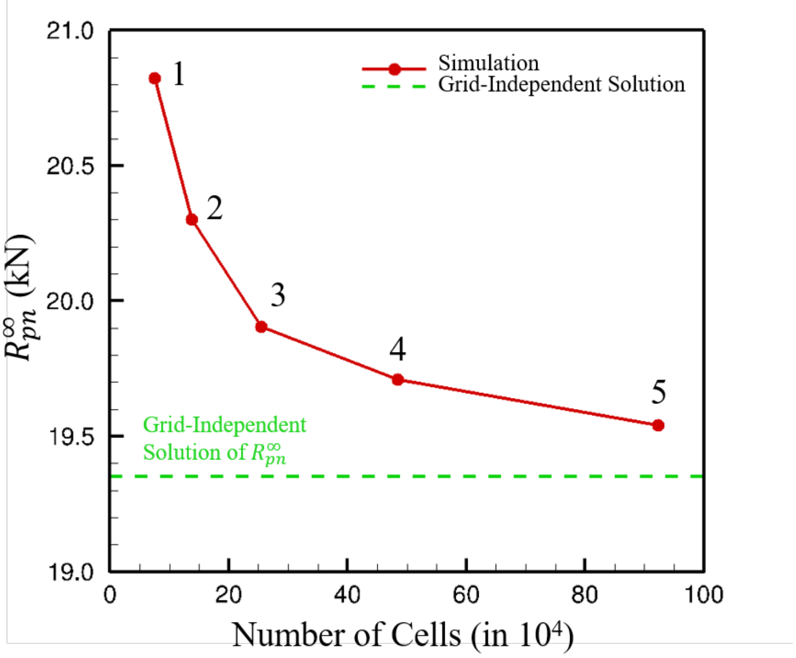

Figure 24 Dependence of Pontoon Resistance on Cell Number

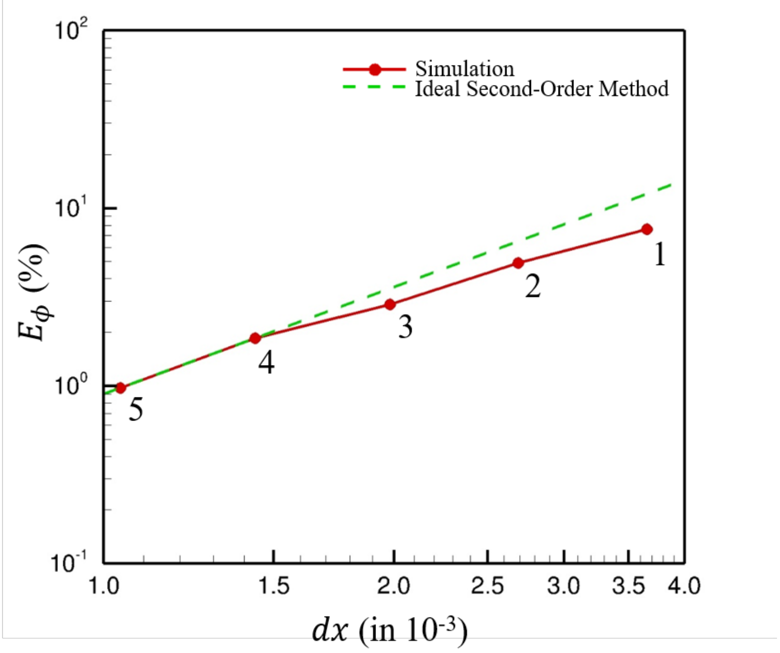

Figure 25 Discretization Error of Pontoon Resistance

4.5 Validation

This section aims to validate the numerical simulation approach by comparing the numerical result of the full-scale ship with that estimated from model tests. The model test is conducted by WOLFSON UNIT in the UK [43]. Due to insufficient longitudinal instability at $Fr = 0.8$ in the experiment, a lower speed of 10 knots ($Fr = 0.34$) is chosen. Table 8 compares the total resistance and the ship's attitude between the model test and CFD calculation.

The position of the center of gravity of a SWATH vessel significantly influences the running trim (θ), as well as resistance. The center of gravity in experiments was not documented in the report, so the difference in the center of gravity could be a significant factor accounting for the difference in the attitude and resistance between the model test and numerical prediction. Although there is a nontrivial resistance difference between CFD calculations and experiment measurements, the predicted free surface pattern is found similar to the experiment result, as shown in Figure 26. The sign convention of the ship's attitude is shown in Figure 27.

Table 8 Comparison between Experiment and Prediction

	R_T (kN)	θ (°)	δ (m)
Experiment	13.8	0.940	-0.048
CFD	11.9	0.309	-0.044
Diff. (%)	14%	67%	8%

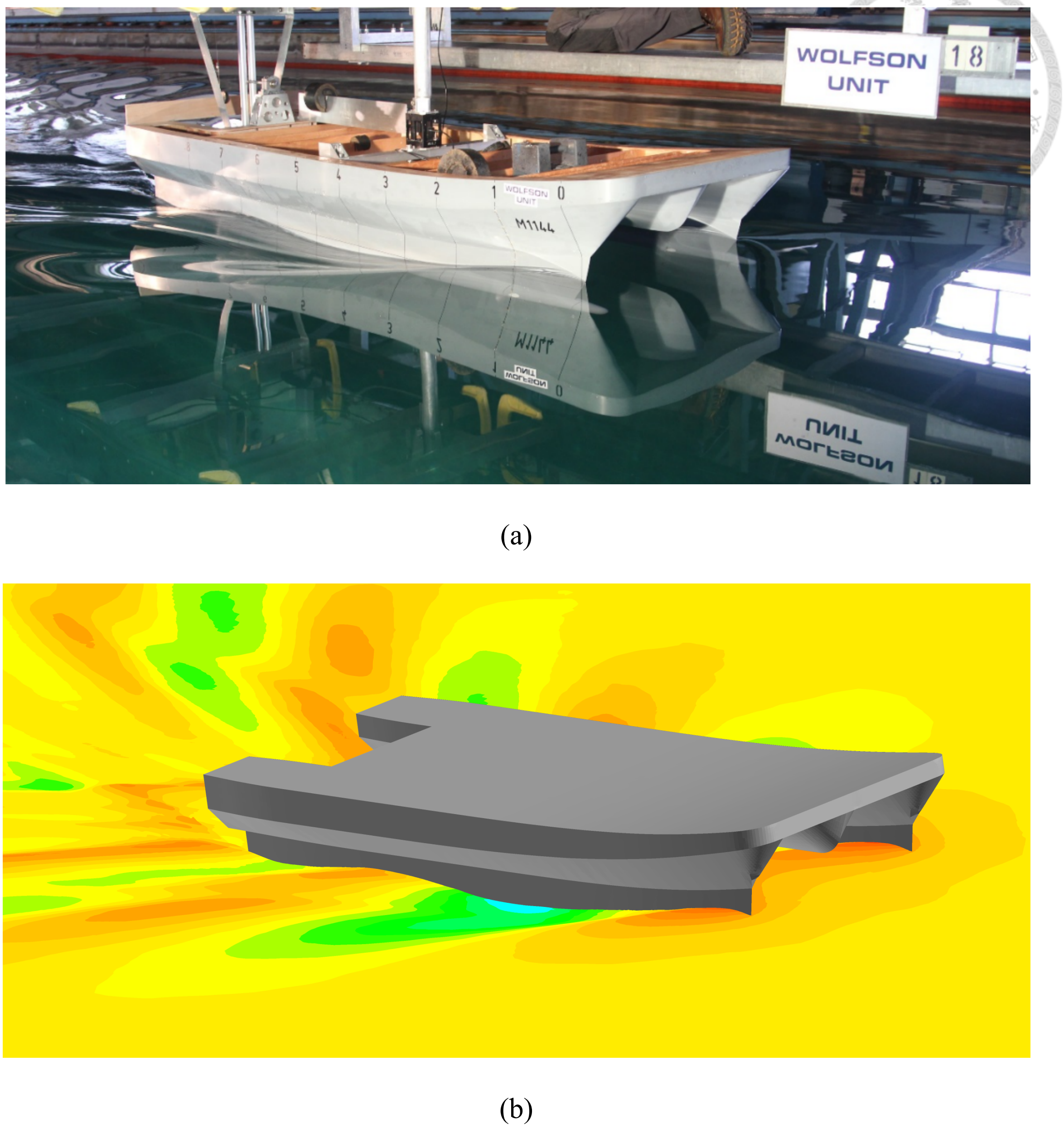

Figure 26 Free Surface Elevation: (a) Experiment [43], (b) CFD

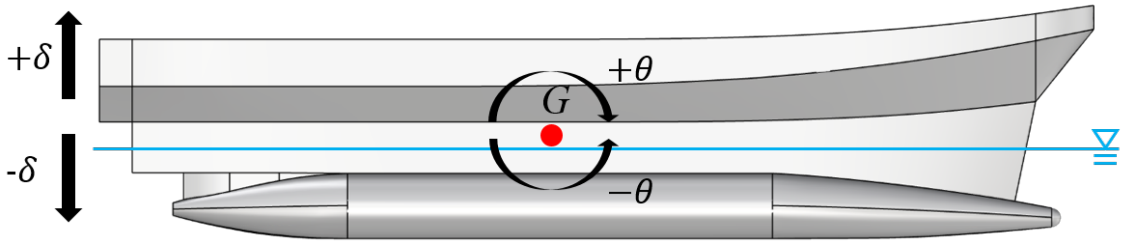

Figure 27 Sign Convention of Ship’s Attitude

4.6 Hardware Platform

Table 9 shows the platform used to predict the ship resistance in fully submerged cases. Each CFD case utilized two computational nodes for parallel processing, with an average computation time of approximately 15 minutes. With a total dataset of 1398 cases, the total time required for CFD simulations is approximately 349.5 hours.

Table 9 Hardware Platform

Software		STARCCM+
Operation System		Linux Centos 7
Central Processing Unit	Model	Intel® Xeon® CPU E5-2673 v2@16 core
	Clock Rate (GHz)	3.3
Random-access Memory		128 GB

doi:10.6342/NTU202304123

Chapter 5 Resistance Prediction

5.1 Case Description

In this study, all cases are classified into different groups based on the fore and aft lengths. Each group has a distinct set of fore and aft lengths. Table 10 provides the group number and the corresponding fore and aft lengths for all cases, where the group numbers are denoted in red. Since some combinations of the fore-body and aft-body angles are unable to define reasonable geometry for a given length set, the number of cases in each group varies. There are 49 groups in total, where each group consist of 16 to 36 cases, and the total number of cases in the dataset is 1398.

Table 10 Different Length Combinations of Pontoon

Group Numbers (G)		L_f (m)						
		1.8	2.8	3.8	4.8	5.8	6.8	7.8
L_a (m)	1.8	1	2	3	4	5	6	7
	2.8	8	9	10	11	12	13	14
	3.8	15	16	17	18	19	20	21
	4.8	22	23	24	25	26	27	28
	5.8	29	30	31	32	33	34	35
	6.8	36	37	38	39	40	41	42
	7.8	43	44	45	46	47	48	49

doi:10.6342/NTU202304123

5.2 Resistance Characteristic of Pontoon

In this section, the influence of the geometric features of the pontoon on its resistance in fully submerged conditions is investigated.

5.2.1 Fixed Length

Figure 28 presents contour plots of resistance for three groups with fixed fore and aft lengths, i.e., Group 7, Group 25, Group 37, and Group 43, under the fully submerged condition. These figures reveal a general trend of increasing resistance with large fore-body and aft-body angles, and decreasing resistance with small fore-body and aft-body angles. Most groups, similar to Group 7, exhibit only one low-resistance region, while some groups have two or three low-resistance regions, suggesting that small fore-body and aft-body angles typically result in better resistance performance. However, some optimized angles are not relatively small when compared to other optimized ones.

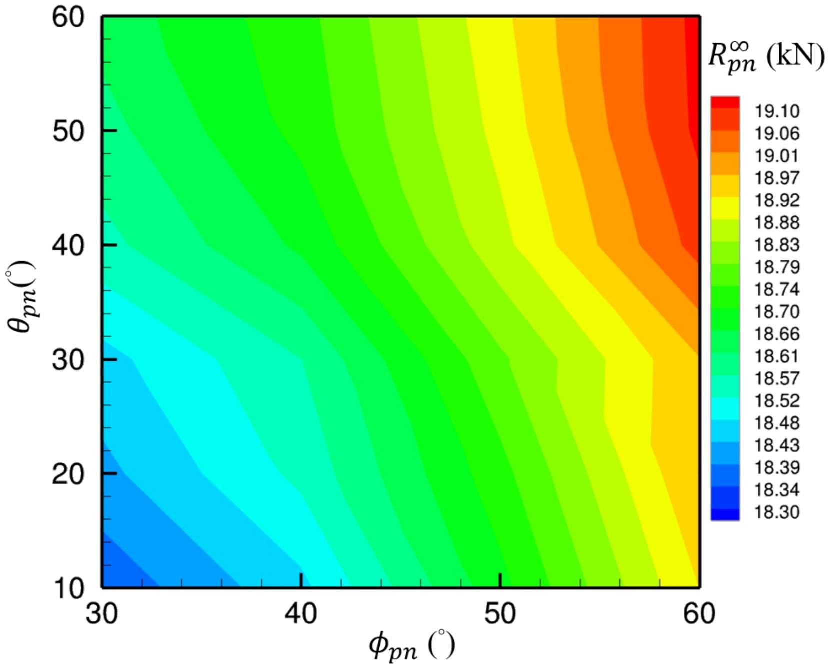

(a)

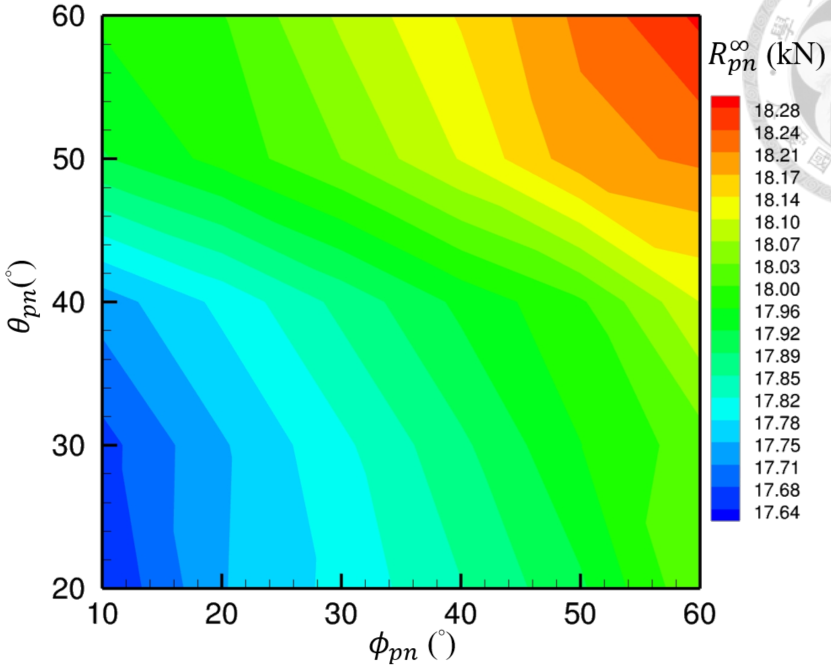
R_{pn}^{∞} (kN)
18.28
18.24
18.21
18.17
18.14
18.10
18.07
18.03
18.00
17.96
17.92
17.89
17.85
17.82
17.78
17.75
17.71
17.68
17.64
$\theta_{pn}(^{\circ})$
60
50
40
30
20
10
20
30
40
50
60
ϕ_{pn} $(^{\circ})$

(b)

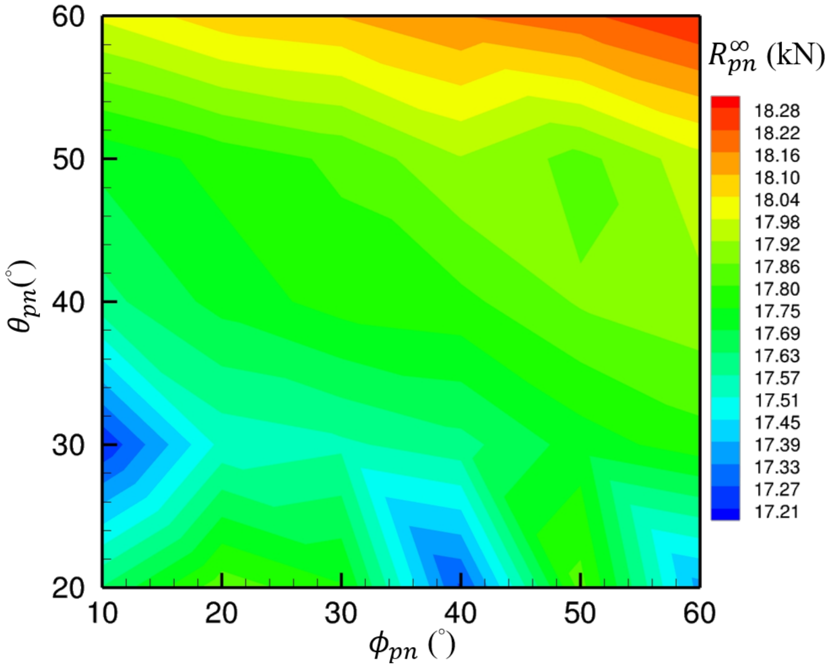
R_{pn}^{∞} (kN)
18.28
18.22
18.16
18.10
18.04
17.98
17.92
17.86
17.80
17.75
17.69
17.63
17.57
17.51
17.45
17.39
17.33
17.27
17.21
$\theta_{pn}(^{\circ})$
60
50
40
30
20
10
20
30
40
50
60
ϕ_{pn} $(^{\circ})$

(c)

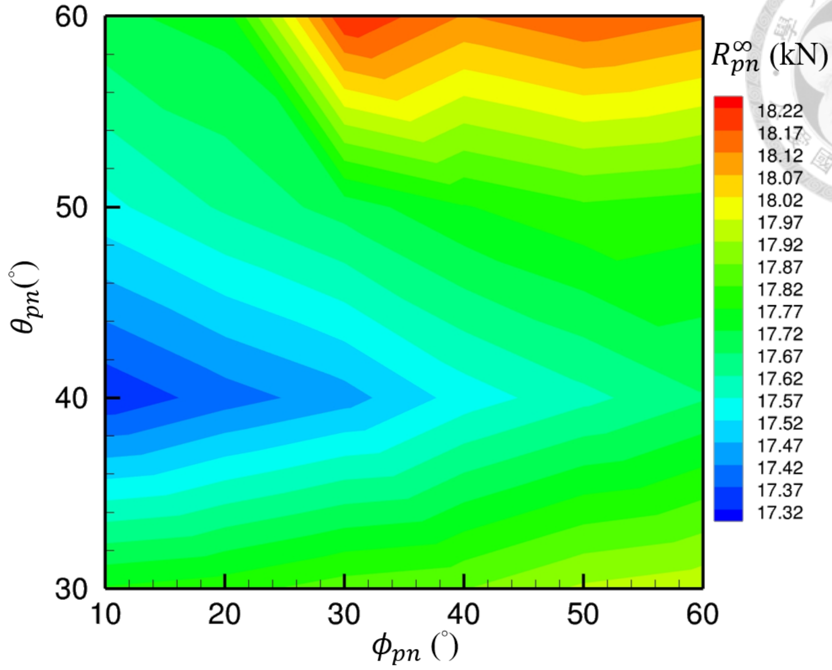

(d)

Figure 28 The Resistance of Pontoon: (a) $G = 7$, (b) $G = 25$, (c) $G = 37$, (d) $G = 43$

5.2.2 Fixed Angle

Figure 29 illustrates the profile lines of three investigated pontoons, with the longitudinal length normalized by L_{pn}. In order to highlight the impact of different fore and aft lengths on resistance, the fore-body and aft-body angles of the compared cases are identical for these three cases. When the fore or aft length is small, the model shape becomes blunt, but it becomes sharp or close to a cone as the fore or aft length increases. Among the three cases, Case 3 has the shortest fore length and the longest aft length, making the model of Case 3 blunter in the fore section and sharper in the aft section. Similarly, Case 1 has the longest fore length and the shortest aft length, and leads to a sharp fore section and a blunt aft section. Table 11 lists the fore and aft lengths, fore-body and aft-body angles, and total resistance for three cases in Figure 29, indicating that a small fore-body of the pontoon leads to a small total resistance. Figure 30 presents the distribution of shear stress and pressure for three cases. Figure 30 (a) shows that a sharp shape change results in the growth of shear force, such as the fore-body of Case 2 and Case 3, and the aft-body of Case 1 and Case 2. Figure 30 (b) shows that a blunt shape generates a negative pressure region near the end, while a sharp one does not.

doi:10.6342/NTU202304123

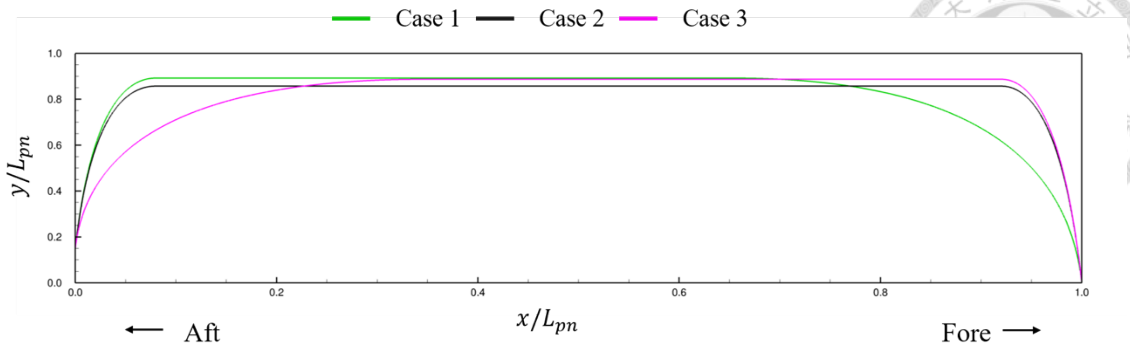

Figure 29 The Profile of Pontoon

Table 11 The Resistance of Pontoon under Immersed Condition

Case	L_f (m)	L_m (m)	L_a (m)	θ_{pn} (°)	ϕ_{pn} (°)	R_{pn}^{∞} (kN)
1	7.8	12.9	1.8	60	60	19.11
2	4.8		4.8			18.28
3	1.8		7.8			18.12

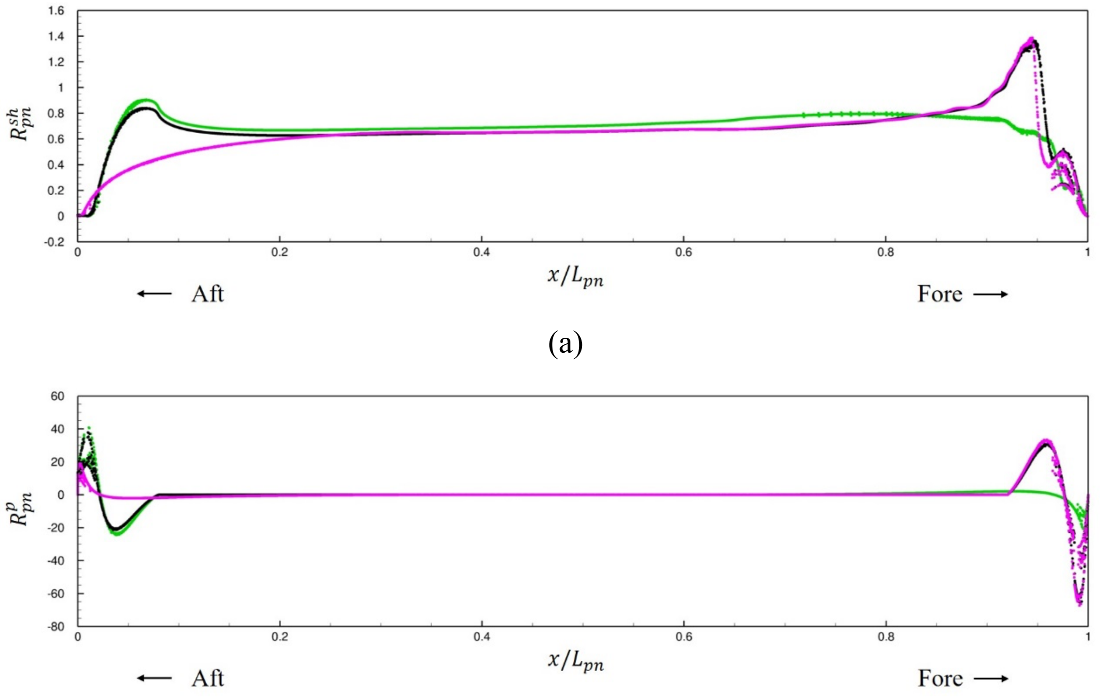

(a)

(b)

Figure 30 The Resistance Distribution of Pontoon: (a) Shear, (b) Pressure

5.3 Correlation between Moment and Resistance

Figure 31 shows the correlation between the total resistance and Munk moment obtained from the CFD simulations, where each red dot represents a case. The figure shows that as the Munk moment approaches zero, the resistance also decreases. This phenomenon indicates that a fin stabilizer is required to balance the Munk moment. As the Munk moment increases, the fin stabilizer needs to operate at a larger angle of attack, leading to high additional resistance. Therefore, the angle of attack of the fin stabilizer is crucial in reducing the resistance.

Figure 32 shows the correlation between LCB and the Munk moment. The graph demonstrates that when LCB is located closer to the stern of the vessel, the Munk moment is reduced. This observation is consistent with previous research on the Munk moment, which suggests that a slender pontoon shape with LCB biased towards the stern is prone to lead to a decreased moment and improved longitudinal stability of the SWATH.

doi:10.6342/NTU202304123

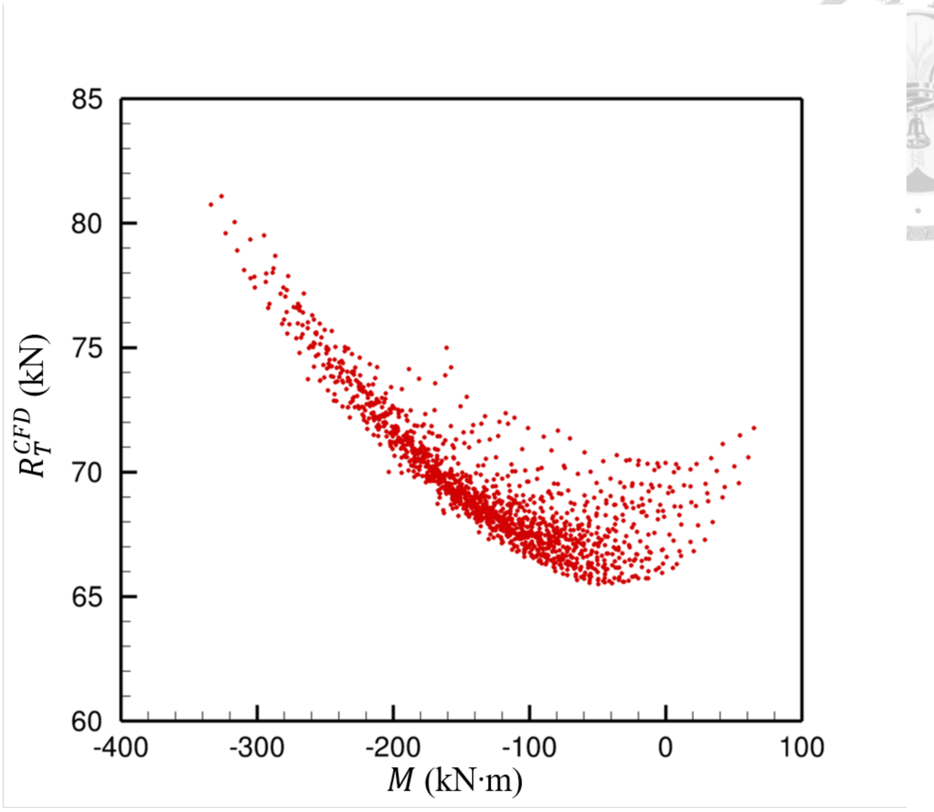

Figure 31 Correlation between the Munk Moment and Resistance

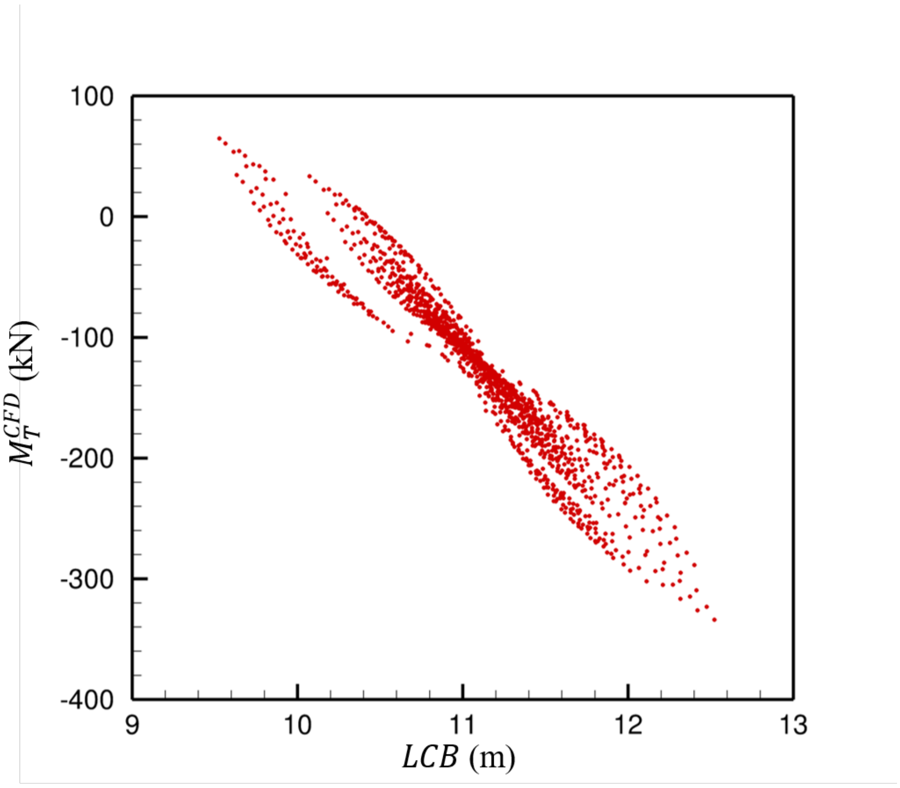

Figure 32 Correlation between LCB and Munk Moment

doi:10.6342/NTU202304123

Chapter 6 DNN Model

6.1 Model Structure

A multi-layer perceptron (MLP), which is a type of deep neural network, consists of three main components: an input layer, hidden layers, and an output layer, as Figure 33. depicted. The classic DNN model can be expressed as follows:

$$y_k^p = g(n_i), \tag{6.1.1}$$

where g is the mapping function, n_i and y_k^p represent the i-th input and the k-th prediction output, respectively.

The DNN model is a forward propagation network. It starts from the input layer and then processes by linear transformation and using a nonlinear transfer function in the hidden layers. The output of each hidden layer is then passed on to the next hidden layer until it reaches the output layer, where the final result or prediction is generated. In linear transformations, the input is multiplied by the weight and then added to the bias. The entire DNN model operates according to the following equations:

$$m_j^{hl} = T(w_{ij}^{hl} n_i + b_j^{hl}), \tag{6.1.2}$$

$$y_k^p = P(w_{jk}^{ol} m_j^{hl} + b_k^{ol}), \tag{6.1.3}$$

where w_{ij}^{hl} and w_{jk}^{ol} respectively represent the weight of the hidden layer and output layer, and b_j^{hl} and b_k^{ol} respectively represent the bias of the hidden layer and output layer, the subscript i corresponds to the i-th input, j corresponds to the j-th neuron, and k corresponds to the k-th output. The transfer function T is the Tansig function, while P is the Purelin function. The equation is as follows:

$$T(n) = \frac{2}{1+e^{-2n}} - 1, \tag{6.1.4}$$

$$P(n) = n. \tag{6.1.5}$$

Next, the predicted value of the neural network, y_k^p, is compared to the predicted value of CFD $\hat{y}_k^p$ in the database, and the loss function e is obtained from the following equation:

$$e = \sum_{k=1}^{r}\left(\hat{y}_k^p - y_k^p\right)^2, \tag{6.1.6}$$

where r is the number of outputs. The loss function is propagated back to the former layer, and the weights and biases are recalculated to obtain new weights and biases. After multiple iterations the loss function between $\hat{y}_k^p$ and y_k^p approaches zero, indicating that the model is successfully trained. This process is called backpropagation, and in this study, Bayesian regularized backpropagation is used.

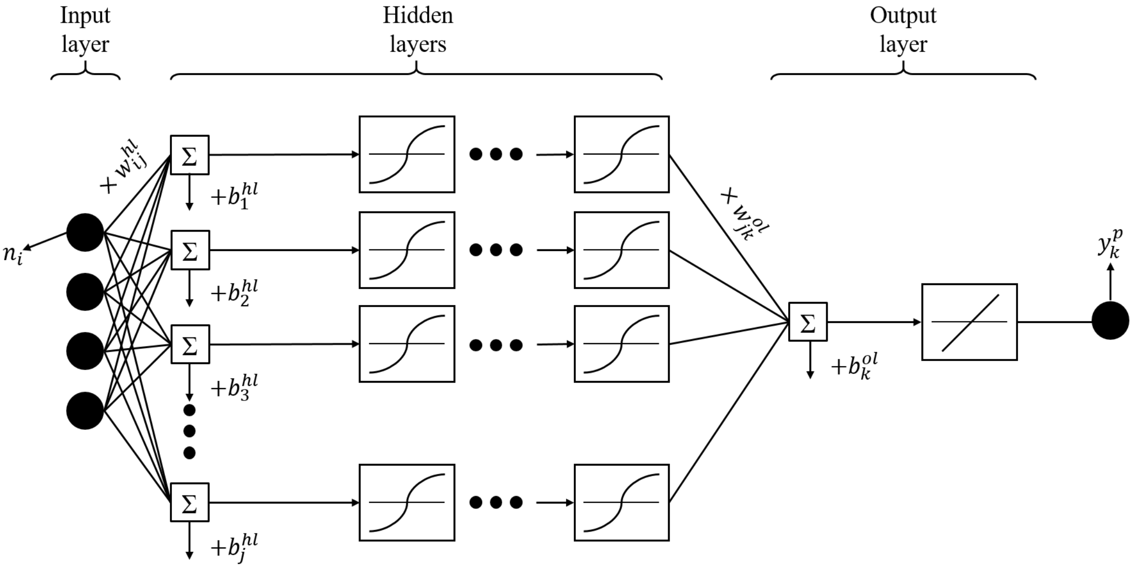

Figure 33 The Structure of the DNN Model

6.2 Model Parameter

In this study, the input and output are four pontoon design parameters and resistance, respectively. Figure 34 shows the framework for establishing the DNN model: First, the minimum and maximum number of layers and neurons are defined. In this study, the DNN model is configured to have a minimum of one hidden layer and a maximum of five hidden layers. The first three layers of the model consist of at least 5 neurons and up to 9 neurons per layer. For other hidden layers, each layer allows to have 3 neurons to 8 neurons. By setting the number of layers and neurons, a total of 4148 different combinations of DNN models are generated, and the best-trained model can be identified among these models. If the best-trained model’s neuron number reaches the prescribed limit, the search range is expanded, and a new round of training is followed. To determine the best-trained model, the mean average percentage error (MAPE) is used as the evaluation metric, and the model with the lowest MAPE is identified as the best-trained model. Lower MAPE values indicate a higher accuracy of the DNN model in predicting the target variable. The MAPE is defined as follows:

$$\mathrm{MAPE} = \frac{1}{r}\sum_{i=1}^{r}\left|\frac{y_k^a - y_k^p}{y_k^a}\right|, \tag{6.2.1}$$

where r represents the total number of data in the database. Figure 35 illustrates the total number of neurons in the hidden layers along with their corresponding MAPE values. Different colors represent distinct total numbers of hidden layers in the models. Generally, as the total number of neurons and hidden layers increases, the achievable lowest MAPE value decreases. However, simply increasing the number of neurons does not guarantee a lower MAPE value.

The best-trained model found in this study has 6, 8, 9, 8, and 7 neurons in each hidden layer as shown in Table 12. After finding the best-trained model, the K-fold cross-validation is employed to ensure the stability of the model. Figure 36 shows the working principle of K-fold cross-validation. The fundamental principle of K-fold cross-validation is to partition the dataset, which consists of 1398 data points, into k non-overlapping subsets, or “folds”, and then train as well as test the data k iterations. In each iteration, the $k-1$ folds are used as the training set, and the remained fold is the testing set. The MAPE of k iterations, as shown in Table 13, is obtained to evaluate the stability of the model.

After the K-fold cross-validation is performed, the model is used for the subsequent prediction and parameter optimization. In addition to the 1398 data points in the original database used for training, this study prepares 80 additional test data points to evaluate the model. When all 1398 data points from the original database are used as training data, the proposed model’s MAPE is 0.19%, as shown in Figure 37. The 80 test data have a MAPE of 0.37%, as depicted in Figure 38. Figure 37 and Figure 38 depict the scatter plots of the DNN predicted values versus the CFD simulated values for the training and testing datasets.

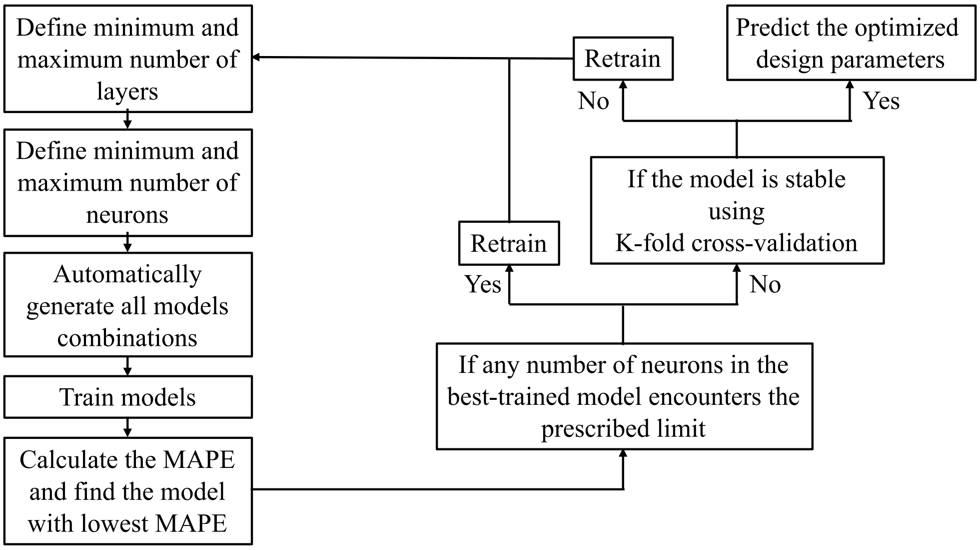

Figure 34 Framework of DNN Model

doi:10.6342/NTU202304123

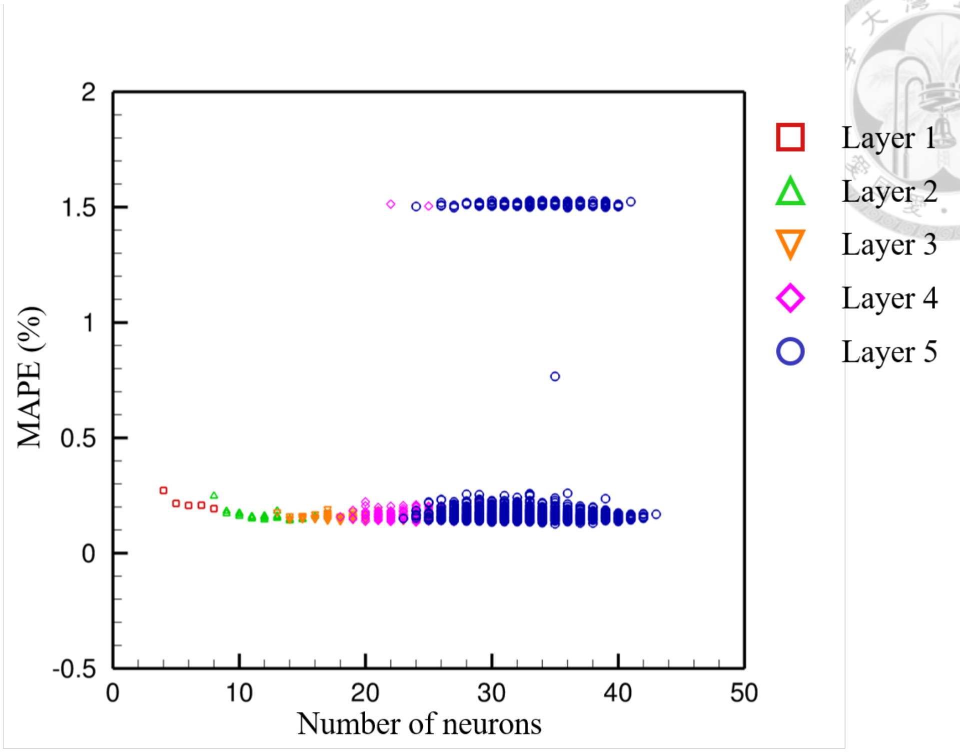

Figure 35 MAPE of DNN Models

Table 12 Proposed DNN Model

Layer No.	1	2	3	4	5
No. of Neuron	6	8	9	8	7

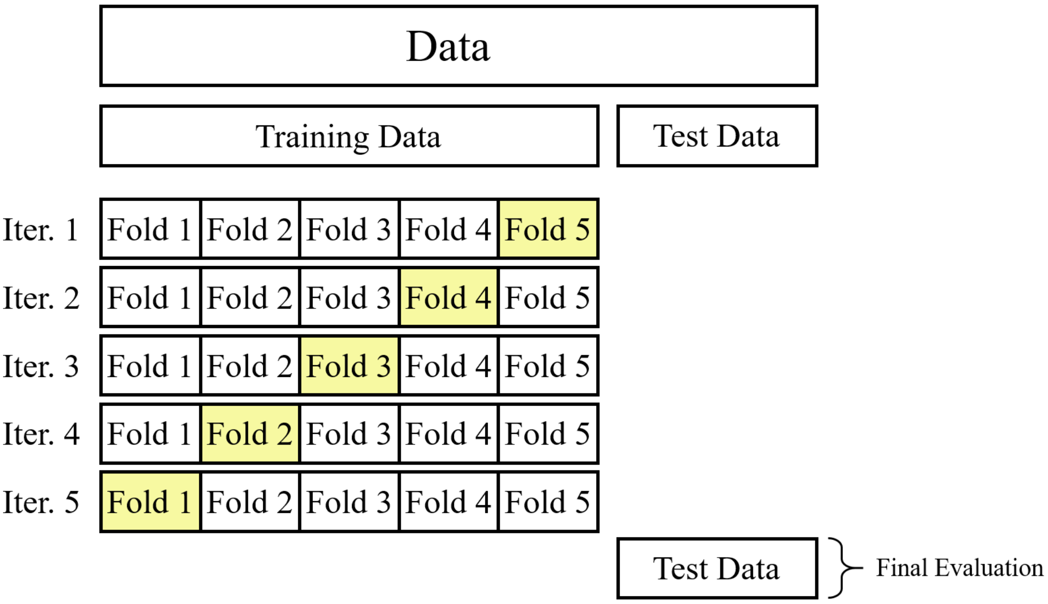

Figure 36 K-fold Cross-validation

doi:10.6342/NTU202304123

Table 13 The MAPE of K-fold Cross-validation

Iteration	1	2	3	4	5	Average
Training MAPE	0.09	0.09	0.09	0.09	0.09	0.09
Test MAPE	0.18	0.21	0.19	0.24	0.26	0.22

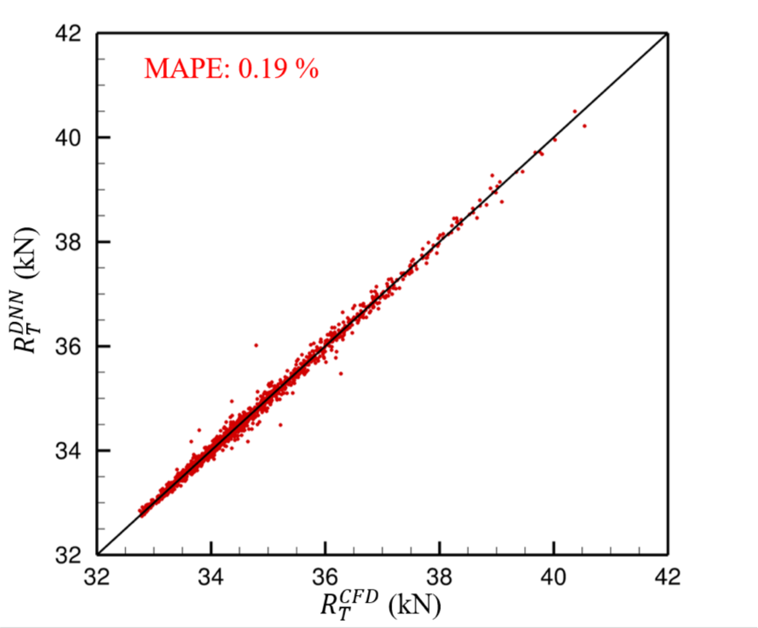

Figure 37 The MAPE of the Proposed DNN Model Using Training Data

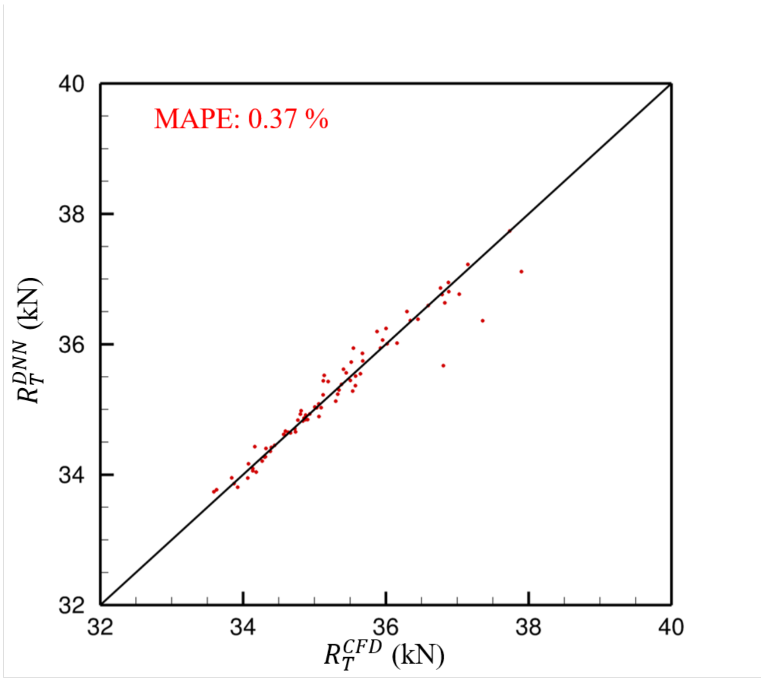

Figure 38 The MAPE of the Proposed DNN Model Using Test Data

6.3 Optimized Parameter Prediction

After the DNN model is proposed, the range of design parameters to be searched for resistance optimization is specified. The range of design parameters is listed in Table 14, and these ranges are determined based on the resistance and moment trends from Figure 31. The target for resistance optimization is set to 0 kN, which means allowing the model to automatically search for the lowest achievable resistance and the corresponding design parameter combination. The DNN model discovers 25 combinations of resistance optimization parameters, and these combinations are then validated using CFD to ensure their effectiveness in achieving resistance optimization.

Table 14 The Range of DNN Prediction of Pontoon

	L_f (m)	L_a (m)	θ_{pn} (°)	ϕ_{pn} (°)
Upper Limit	5.8	3.8	20	10
Lower Limit	7.8	7.8	60	30
Intervals	0.2	0.2	5	5

doi:10.6342/NTU202304123

6.4 Hardware Platform

Table 15 shows the platform used to train the DNN model. The DNN model is trained using the commercial software MATLAB, utilizing a single core for training. Parallel processing is not employed due to the limited number of layers and neurons. The total number of trained models is 4148, with a training time of approximately 10 hours. The time cost to predict the optimized design parameter combinations is around 3 minutes.

Table 15 Hardware Platform

Software		MATLAB
Operation System		Windows10
Central Processing Unit	Model	Intel® Core™ i9-9980XE@18 core
	Clock Rate (GHz)	3.0
Random-access Memory		128 GB

Chapter 7 Pontoon Optimization

7.1 Hull Form and Resistance

With the implementation of the DNN model, the optimized pontoon design of the SWATH vessel is obtained. Table 16 lists the optimized design parameters, as well as the parameters of the baseline. Since the pontoon design of the baseline is not axisymmetric, some geometric parameters are unavailable. Figure 39 and Figure 40 show the side view and the line drawing of the baseline design and optimized design, respectively. In terms of shape, the optimized design has a shorter aft-body but a longer fore-body, and LCB is located at 12.13 meters, which is closer to the stern than the baseline design. Therefore, it is expected to obtain a smaller Munk moment.

Due to the difference between hull forms, the longitudinal moment of the optimized design is better than the baseline. So a decrease in the airfoil's angle of attack, results in a reduction in the resistance. Table 17 and Table 18 show the simulation result of the optimized and baseline design, where the M_{pn}^{fs} is the longitudinal moment of the pontoon, R_T^{DNN} and R_T^{CFD} are the total resistance of SWATH predicted by DNN model and by CFD, respectively, where α_{fore} is the fore fin stabilizer's angle of attack. This study uses moment interpolation among different fin stabilizer angles to find the zero moment condition, where R_{st}^{fs}, R_{pn}^{fs}, R_{fore}^{fs}, and R_{aft}^{fs} are the resistances of the strut, pontoon, fore fin stabilizer, and aft fin stabilizer, respectively, with the superscript fs representing the free surface flow field. M_{pn}^{fs} of the optimized design is much smaller than that of the baseline because of the shape of the pontoon. There is a discrepancy between the total resistance predicted by DNN and CFD. This discrepancy arises from the linearization of resistance components. Nevertheless, it is important to note that the resistance trend

doi:10.6342/NTU202304123

observed between the optimized design and baseline design is quite similar. This indicates that resistance decoupling is capable of capturing resistance trends despite the errors between the two prediction methods. The pontoon resistance (R_{pn}^{fs}) of the optimized design is 8.6% higher than the baseline design, as the optimized design has a little larger volume than the baseline design. Due to a significant reduction in the fin resistance of the optimized design, the total resistance of the optimized design is still better than the baseline design. The total resistance reduction of the optimized design is 2.2% when compared to the baseline design.

Figure 41 shows the comparison of the free surface elevation, while Figure 42 displays the comparison of pressure distribution of the flow field and on the hull surface. From Figure 41, it can be observed that the optimized design has a higher wave height than the baseline design. From Figure 42, it can be seen that the pressure distribution on the hull surface of the optimized design is smoother than on the baseline design. There are no abrupt low-pressure regions on the hull surface because the pontoon of the optimized design has a smooth curvature distribution.

Figure 43 shows the position of the propeller disk. The centers of the propeller disk for optimized and baseline design are (1.39, 3.77 -1.2) and (1.39, 3.77, -1.44), respectively. The normalized velocity components are defined by (7.1.1), and the nominal wake (ω_n) is defined by (7.1.2):

$$V_i^* = \frac{v_i}{V_s}, \tag{7.1.1}$$

$$\omega_n = 1 - V_A^* \tag{7.1.2}$$

Figure 44 defines the normalized velocity component of the propeller disk, where V_A^* is the axial velocity, V_R^* is the radial velocity, V_T^* is the tangential velocity. θ_p is the azimuthal angle, and R_p is the radius of the propeller. Figure 45 shows the nominal wake

doi:10.6342/NTU202304123

of the propeller disk, and Figure 46 shows the normalized velocity component of the propeller disk. The nominal wake of the baseline design is 0.13, and that of the optimized design is 0.24. Although the optimized design demonstrates improved performance in terms of the resistance and Munk moment, it delivers a worse wake when compared to the baseline design. This has an adverse effect on the propulsion performance.

doi:10.6342/NTU202304123

Table 16 Geometric Parameters of Baseline and Optimized Design

Hull Form	L_f (m)	L_m (m)	L_a (m)	θ_{pn} (˚)	ϕ_{pn} (˚)
Baseline	7.54	11.12	4.56	N/A	N/A
Optimized	7.8	7.9	6.8	10	35

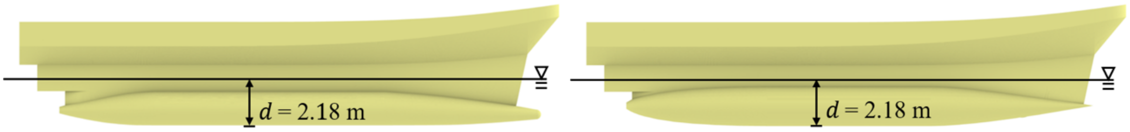

(a) (b)

Figure 39 The Side View of Hull Form: (a) Baseline Design, (b) Optimized Design

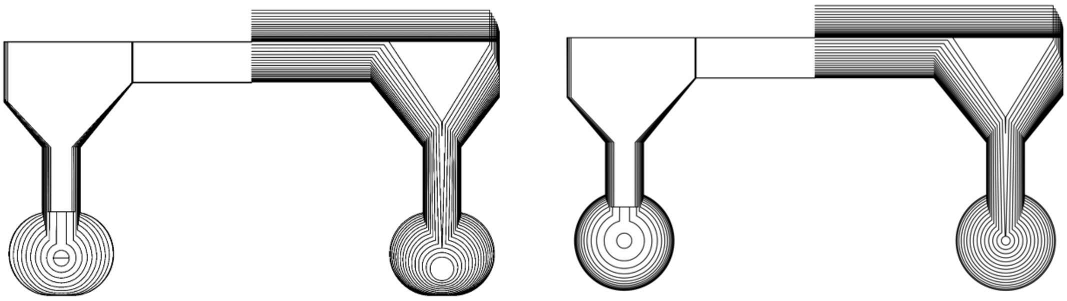

(a) (b)

Figure 40 Line Drawing of Hull Form: (a) Baseline Design, (b) Optimized Design

Table 17 The Longitudinal Moment of Baseline and Optimized Design

Hull Form	LCB (m)	M_{pn}^{fs} (kN·m)	α_{fore} (˚)
Baseline	12.88	239.45	10.31
Optimized	12.13	52.72	2.51

Table 18 The Resistance Components of Baseline and Optimized Design (Force in kN)

Hull Form	R_T^{DNN}	R_T^{CFD}	R_{st}^{fs}	R_{pn}^{fs}	R_{fore}^{fs}	R_{aft}^{fs}	R_{ss}^{fs}
Baseline	69.12	104.65	25.19	68.57	7.28	2.57	1.01
Optimized	65.36	102.37	21.18	74.76	3.27	2.36	0.77
Difference (%)	5.5	2.2	17.3	-8.6	89.4	76.0	27.0

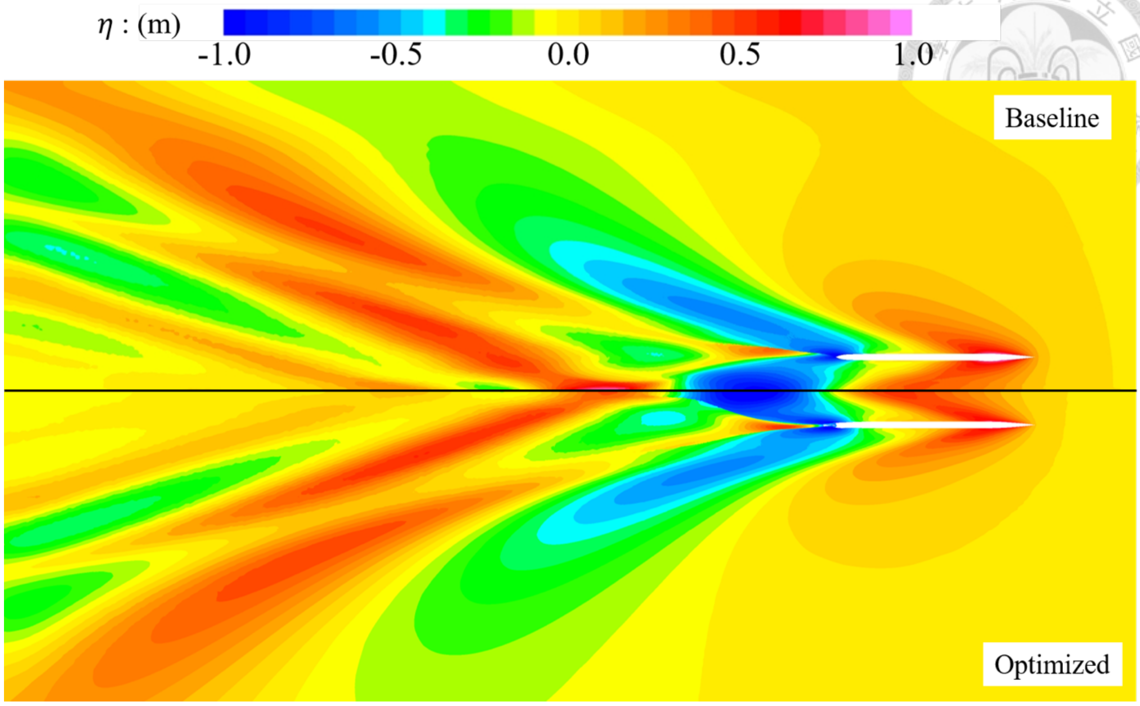

Figure 41 Free Surface Elevation of Baseline and Optimized Design

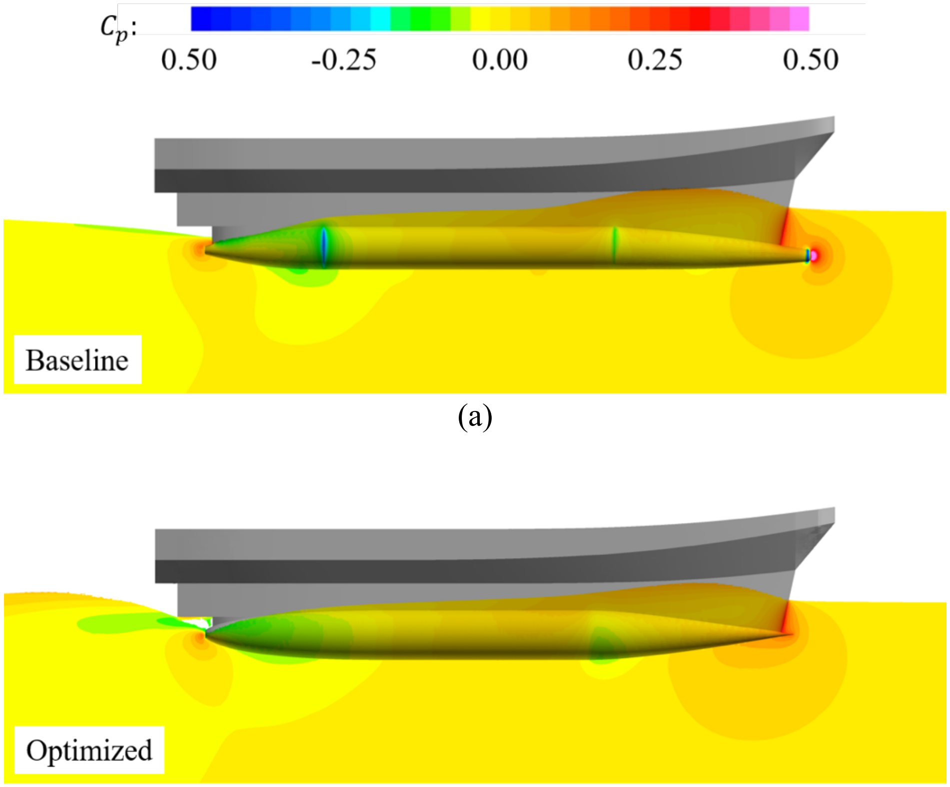

(a)

(b)

Figure 42 Pressure Distribution of Hull Form: (a) Baseline Design, (b) Optimized Design

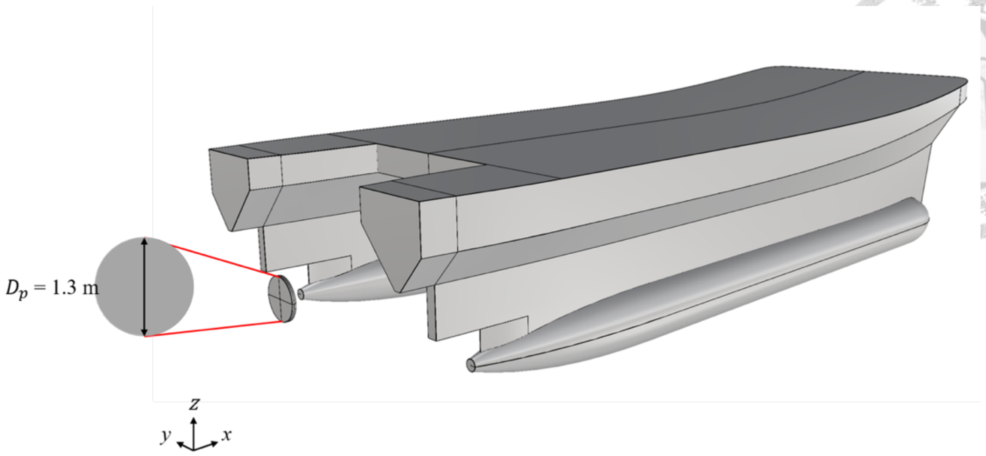

Figure 43 Position of Propeller

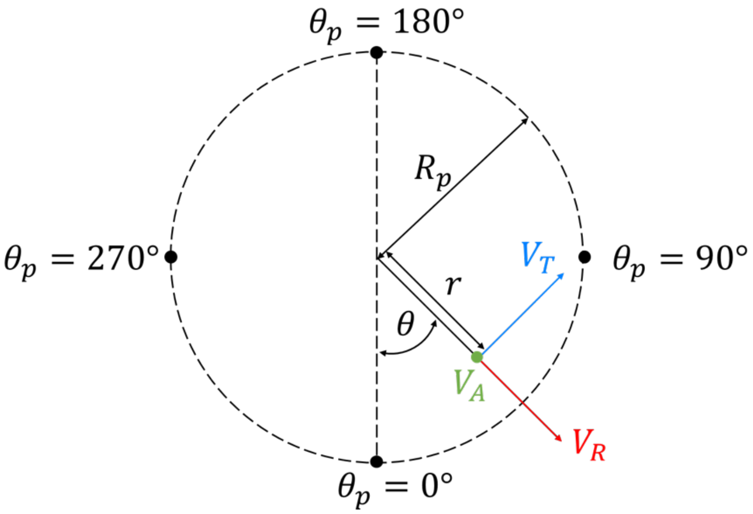

Figure 44 Definition of Velocity Component of Propeller Disk

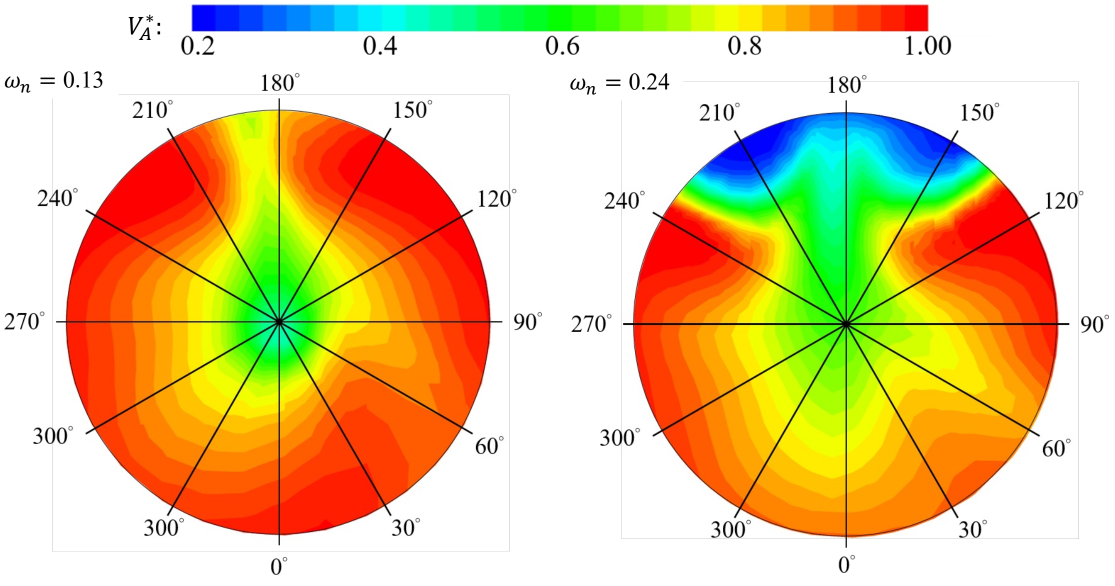

(a)

(b)

Figure 45 Nominal Wake of Hull Form: (a) Baseline design, (b) Optimized design

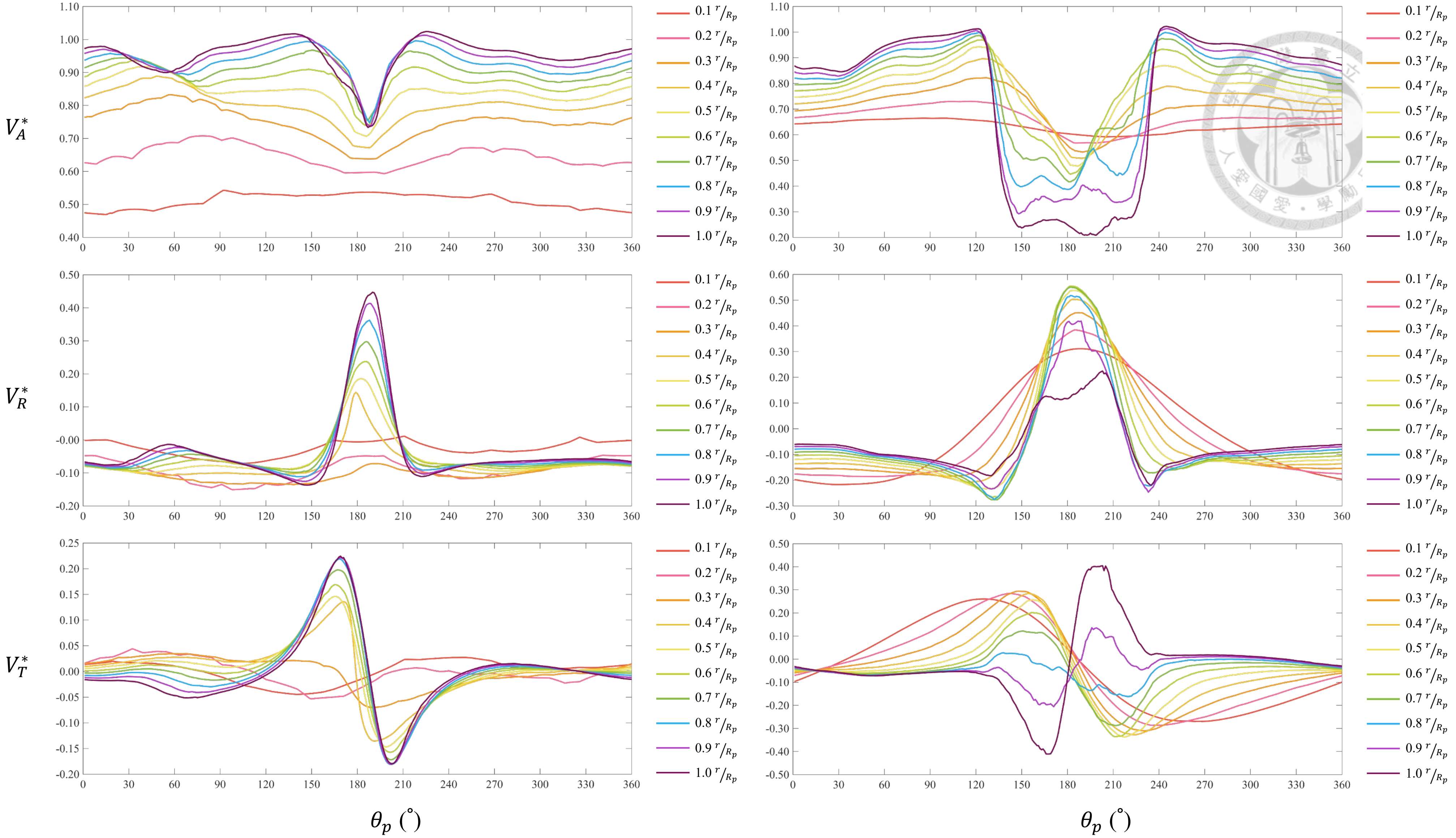

Figure 46 Velocity Component of Propeller Plane: Baseline Disk (left) and Optimized Design (right)

doi:10.6342/NTU202304123

7.2 Total Resistance in Full Speed Range

In the previous section, an optimized hull form is proposed for a specific speed, which is $Fr = 0.8$. Therefore, this section investigates the performance of still water resistance at other speeds. The considered speed range is $Fr = 0.2$ to 0.8.

When the resistance performance across the full speed range is investigated, fixed-running simulations are used, and the angle of the fin stabilizer is estimated using the balance of moment. The estimated angles of the fin stabilizer are listed in Table 19. Figure 47 (a) illustrates the bare hull resistance, while Figure 47 (b) illustrates the resistance including the fin stabilizer. When the fin stabilizer is not considered, the baseline design generally performs better in all speed ranges. However, when the fin stabilizer is taken into account, the optimized design exhibits better performance at high speeds. It is important to note that at high speeds, the absence of a fin stabilizer would lead to longitudinal instability and the risk of capsizing. As a result, the optimized design maintains an advantage at high speeds due to the fin stabilizer. The advantage resulting from the hull moment reduction can be observed in Figure 48, where the moment of the optimized design is consistently better across all Froude numbers.

doi:10.6342/NTU202304123

Table 19 Angle of Fin Stabilizer

Froude Number	0.2	0.3	0.4	0.5	0.6	0.7	0.8
Baseline (°)	2.5	2.5	7.5	2.0	9.0	15.0	20.5
Optimized(°)	1.0	1.5	2.0	9.0	4.0	3.0	6.0

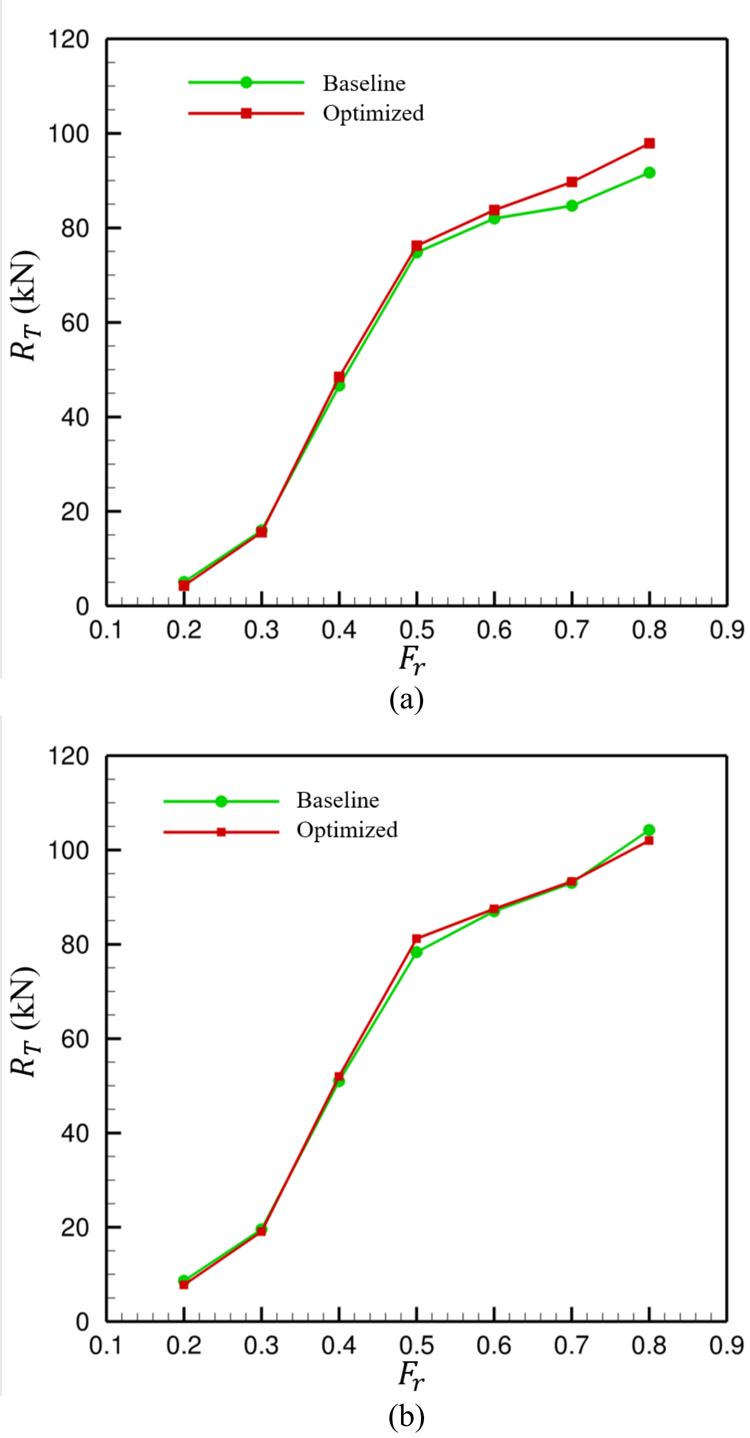

(a)

(b)

Figure 47 Total Resistance at Different Speed: (a) Bare hull, (b) with Fin Stabilizers

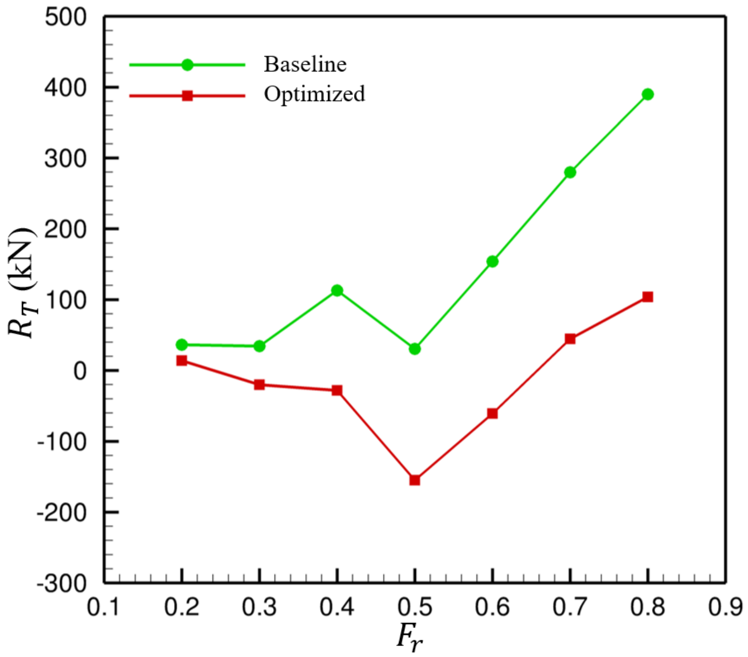

Figure 48 Hull Moment at Different Speed: (a) Bare hull, (b) with Fin Stabilizers

doi:10.6342/NTU202304123

Chapter 8 Conclusion

8.1 Conclusion

This study proposes a parameterized SWATH underwater pontoon design method, which involves resistance analysis and the application of a DNN model to identify an optimized design with reduced total resistance and moment.

To simplify the calculations, this study decomposes the resistance of the SWATH into the resistance contributions from the pontoon, strut, superstructure, and fin stabilizers. Among these, the pontoon contributes the largest portion of the resistance, making it the primary target for optimization. The pontoon design is based on an axisymmetric body, and its design parameters include the lengths and angles at the fore and aft bodies. After the pontoon resistance optimization, CFD is employed to predict the total resistance of SWATH in a three-dimensional flow field as the final validation step.

During the resistance optimization, a DNN model is utilized. The proposed model comprises five hidden layers with 6, 8, 9, 8, and 7 neurons, respectively, and the MAPE is measured at 0.19%. The optimized parameters suggested by the DNN model are a forebody length of 7.8 meters, an aft-body length of 6.8 meters, a fore angle of 10 degrees, and an aft angle of 35 degrees. The LCB of the optimized design is closer to the stern compared to the baseline design. Additionally, the moment has reduced by 127.8%, and the angle of the fin stabilizer has decreased by 121.7%. After the resistance of all components of SWATH is taken into consideration, the total resistance of SWATH has decreased by 2.2%.

In the comparison of the resistance performance at different speeds, it is evident that the proposed optimized design performs better at high speeds. This is attributed to the significant reduction in the Munk moment, resulting in a small angle of attack for the

doi:10.6342/NTU202304123

stabilizer and reduced fin drag.

In summary, to prevent longitudinal instability and potential capsizing, it is crucial to minimize the moment when designing the pontoon. This way not only enhances safety but also reduces the resistance.

8.2 Future Work

While a linearization method proposed in this study can reduce the computational cost to predict optimized parameters, nonlinear models are obviously capable of reducing the errors arising from the linearization. Therefore, in the future, resistance prediction in a three-dimensional flow field is recommended. Furthermore, the proposed optimized design's performance at low speeds is relatively poor, necessitating further exploration of robust methods that can consider the resistance performance across the full speed range. Since the wake performance is also worse in the proposed design than the baseline design, it is essential to propose a design method that can also consider the wake characteristics. Lastly, regarding the application of the DNN model, a multi-objective function model is suggested because SWATH optimization requires considering both resistance and the Munk moment simultaneously.

doi:10.6342/NTU202304123

doi:10.6342/NTU202304123

REFERENCE

[1] G. W. E. Council, "GWEC | Global Wind Report 2021," 2021.

[2] Y. Dalgic, I. Lazakis, and O. Turan, "Investigation of Optimum Crew Transfer Vessel Fleet for Offshore Wind Farm Maintenance Operations," *Wind Engineering,* vol. 39, no. 1, pp. 31-52, 2015. [Online]. Available: https://www.jstor.org/stable/90006858.

[3] F. Pérez Arribas and J. Calderon Sanchez, "A Parametric Methodology for the Preliminary Design of SWATH Hulls," *Ocean Engineering,* vol. 197, 02/01 2020, doi: https://doi.org/10.1016/j.oceaneng.2019.106823.

[4] Y. Lin, Q. Yang, and G. Guan, "Automatic Design Optimization of SWATH Applying CFD and RSM Model," *Ocean Engineering,* vol. 172, pp. 146-154, 01/15 2019, doi: https://doi.org/10.1016/j.oceaneng.2018.11.044.

[5] S. Brizzolara and G. Vernengo, "Automatic Optimization Computational Method for Unconventional S.W.A.T.H. Ships Resistance," *International Journal of Mathematical Models and Methods in Applied Sciences,* vol. 5, pp. 882-889, 01/01 2011.

[6] E. Begovic, C. Bertorello, and S. Mancini, "Hydrodynamic Performances of Small Size Swath Craft," *Brodogradnja,* vol. 66, pp. 1-22, 12/31 2015.

[7] J. H. Ferziger, M. Perić, and R. L. Street, *Computational Methods for Fluid Dynamics by Joel H. Ferziger, Milovan Perić, Robert L. Street*, 4th 2020. ed. Cham: Springer International Publishing, 2020.

[8] Q. Yang, Y. Lin, and G. Guan, "Improved Sequential Sampling for Meta-Modeling Promotes Design Optimization of SWATH," *Ocean Engineering,* vol. 198, 02/15 2020, doi: https://doi.org/10.1016/j.oceaneng.2020.106958.

[9] M. Collette, W. M. Lin, and J. Li, *Applying Advanced Simulation in Early Stage Unconventional Ship Design*. 2010, pp. 344-351.

[10] "Coastal Ocean Mapping Aboard the NOAA Ship Ferdinand R. Hassler." https://oceanexplorer.noaa.gov/okeanos/explorations/acumen12/hassler/welcome.html

[11] A. H. M. D. Ltd. https://www.adhocmarinedesigns.co.uk/latest (accessed.

[12] l. martin. "Historical Programs - Sea Shadow." https://www.lockheedmartin.com/en-us/news/features/history/sea-shadow.html

[13] S. Brizzolara, M. Bovio, A. Federici, and G. Vernengo, "Hydrodynamic Design of a Family of Hybrid SWATH Unmanned Surface Vehicles," *11th International Conference on Fast Sea Transportation, FAST 2011 - Proceedings,* 01/01 2011.

[14] G. Zaraphonitis, A. Papanikolaoy, and M. Androulakakis, "Preliminary Design of a High-Speed SWATH Passenger/Car Ferry," *Marine Technology,* vol. 28, pp. 129-141, 06/01 1991.

[15] P. Macedo, "SWATH SOV Hull Concept and Optimisation for Seakeeping," 2018.

[16] A. Ali, A. Maimun, and Y. Mohamed Ahmed, "Analysis of Resistance and Generated Wave around Semi SWATH Hull at Deep and Shallow Water," *Journal of Advanced Research in Fluid Mechanics and Thermal Sciences,* vol. 58, no. 2, pp. 247-260, 12/16 2020. [Online]. Available: https://akademiabaru.com/submit/index.php/arfmts/article/view/2586.

[17] 葛緯楨、郭值學，〈小水線面船的運動穩定性〉，中國造船，第3卷，頁30-36，2000。

[18] 董祖舜、董文才，〈小水線面雙體船縱向運動穩定性的簡化判據及分析〉，

中國造船，第 4 卷，頁 36-48，1994。

[19] P. Renaud, M. Sacher, and Y.-M. Scolan, "Multi-objective hull form optimization of a SWATH configuration using surrogate models," *Ocean Engineering,* vol. 256, 2022/07/15/ 2022, doi: https://doi.org/10.1016/j.oceaneng.2022.111209.

[20] A. C. Fairlie-Clarke, "Regression Analysis of Ship Data," *International Shipbuilding Progress,* vol. 22, pp. 227-250, 1975, doi: 10.3233/ISP-1975-2225101.

[21] J. Holtrop and G. G. J. Mennen, "An Approximate Power Prediction Method," *International Shipbuilding Progress,* vol. 29, pp. 166-170, 1982, doi: 10.3233/ISP-1982-2933501.

[22] P. Wang, Z. Chen, and Y. Feng, "Many-Objective Optimization for a Deep-Sea Aquaculture Vessel Based on an Improved RBF Neural Network Surrogate Model," *Journal of Marine Science and Technology,* vol. 26, no. 2, pp. 582-605, 06/01 2021, doi: 10.1007/s00773-020-00756-z.

[23] Y. Wang, J. Joseph, T. P. Aniruddhan Unni, S. Yamakawa, A. Barati Farimani, and K. Shimada, "Three-Dimensional Ship Hull Encoding and Optimization via Deep Neural Networks," *Journal of Mechanical Design,* vol. 144, no. 10, 2022, doi: 10.1115/1.4054494.

[24] D. C. Yu and L. Wang, "Hull Form Optimization with Principal Component Analysis and Deep Neural Network," *ArXiv Preprint* 2018.

[25] J. H. Kim *et al.*, "Prediction of the Superiority of The Hydrodynamic Performance of Hull Forms Using Deep Learning," *International Journal of Naval Architecture and Ocean Engineering,* vol. 14, 2022.

[26] M. Mittendorf, U. D. Nielsen, and H. B. Bingham, "The Prediction of Sea State Parameters by Deep Learning Techniques using Ship Motion Data," in *7th World Maritime Technology Conference 2022*, 2022.

[27] C. P. Tsai, C. Lin, and J. N. Shen, "Neural Network for Wave Forecasting Among Multi-Stations," *Ocean Engineering,* vol. 29, no. 13, pp. 1683-1695, 10/01 2002, doi: https://doi.org/10.1016/S0029-8018(01)00112-3.

[28] P. Romero Tello, J. E. Gutiérrez Romero, and B. Serván Camas, "Prediction of Seakeeping in the Early Stage of Conventional Monohull Vessels Design Using Artificial Neural Network," *Journal of Ocean Engineering and Science,* 06/18 2022, doi: https://doi.org/10.1016/j.joes.2022.06.033.

[29] Y. C. Liu, W. Y. Duan, L. M. Huang, S. L. Duan, and X. W. Ma, "The Input Vector Space Optimization for LSTM Deep Learning Model in Real-Time Prediction of Ship Motions," *Ocean Engineering,* vol. 213, 10/01 2020, doi: https://doi.org/10.1016/j.oceaneng.2020.107681.

[30] M. Rashid, J. Zhang, and M. Zhao, *Real-Time Ship Motion Forecasting Using Deep Learning*. 2021, pp. 1-5.

[31] E. Rizzuto and V. Ruggiero, "Deep Neural Network (DNN) Method to Predict the Displacement Behavior of Neutral Axis for Ships in Vertical Bending," in *Technology and Science for the Ships of the Future: Proceedings of NAV 2022: 20th International Conference on Ship & Maritime Research*, 2022, vol. 6: IOS Press, p. 95.

[32] H. Cui, O. Turan, and P. Sayer, "Learning-based Ship Design Optimization Approach," *Computer-Aided Design,* vol. 44, no. 3, pp. 186-195, 03/01 2012, doi: https://doi.org/10.1016/j.cad.2011.06.011.

[33] J. Khairuddin, A. Maimun, K. Hiekata, C. L. Siow, and A. Ali, "Web Application with Data Centric Approach to Ship Powering Prediction Using Deep Learning,"

Software Impacts, vol. 11, 2022.

[34] J. B. Lee, M. I. Roh, and K. S. Kim, "Prediction of Ship Power Based on Variation in Deep Feed-Forward Neural Network," *International Journal of Naval Architecture and Ocean Engineering,* vol. 13, pp. 641-649, 01/01 2021, doi: https://doi.org/10.1016/j.ijnaoe.2021.08.001.

[35] L. Lei, Z. Wen, and Z. Peng, "Prediction of Main Engine Speed and Fuel Consumption of Inland Ships Based on Deep Learning," in *Journal of Physics: Conference Series*, 2021, vol. 2025, no. 1: IOP Publishing.

[36] S. H. Kim, "A Study on the Method for the Estimation of Energy Efficiency Operational Indicator of a Ship Based on Technologies of Big Data and Deep Learning," Seoul National University, 2018.

[37] B. Sener, O. Pedgley, P. Wormald, and I. Campbell, "Incorporating the Freeform Haptic Modelling System into New Product Development," in *Proceedings of the EuroHaptics conference*, 2003.

[38] K. Lagios, J. Niemasz, and C. F. Reinhart, "Aminated Building Performance Simulation (ABPS) – Linking Rhinoceros/Grasshopper with Radiance/Daysim," 2010.

[39] J. Niemasz, J. Sargent, and C. Reinhart, *Solar Zoning and Energy in Detached Dwellings*. 2011, pp. 37-45.

[40] L. Yun, A. Bliault, and H. Z. Rong, *High Speed Catamarans and Multihulls Technology, Performance, and Applications / by Liang Yun, Alan Bliault, Huan Zong Rong*, 1st 2019. ed. New York, NY: Springer New York, 2019.

[41] O. G. Tietjens, *Fundamentals of Hydro- and Aeromechanics; Based on Lectures of L. Prandtl. Translated by L. Rosenhead* (Engineering Societies Monographs.). New York: Dover Publications, 1957.

[42] H. Söding, *Manoeuvring Technical Manual Part 2*. 2019, pp. 74-95.

[43] "Towing Tank Tests in Support of the Design of a 26m SWATH."

doi:10.6342/NTU202304123